CC BY-NC

THCM numerical simulations of the engineered barrier system for radioactive waste disposal

- Javier Samper, PhD
- CICA, Centro de Investigaciones Científicas Avanzadas, E.T.S. Ingenieros de Caminos, Canales y Puertos, Campus de Elviña, Universidade de A Coruña, 15071 A Coruña
- ORCID number: 0000-0002-9532-8433
- Alba Mon, PhD
- CICA, Centro de Investigaciones Científicas Avanzadas, E.T.S. Ingenieros de Caminos, Canales y Puertos, Campus de Elviña, Universidade de A Coruña, 15071 A Coruña
- ORCID number: 0000-0003-2908-5928
- Luis Montenegro, PhD
- CICA, Centro de Investigaciones Científicas Avanzadas, E.T.S. Ingenieros de Caminos, Canales y Puertos, Campus de Elviña, Universidade de A Coruña, 15071 A Coruña
- ORCID number: 0000-0003-2737-1437
- Acacia Naves, PhD
- CICA, Centro de Investigaciones Científicas Avanzadas, E.T.S. Ingenieros de Caminos, Canales y Puertos, Campus de Elviña, Universidade de A Coruña, 15071 A Coruña
- ORCID number: 0000-0003-1897-0884

Corresponding author: j.samper@udc.es

Abstract (148 words)

The final disposal of high-level radioactive waste in geological repositories envisages an engineered barrier system (EBS) with a bentonite buffer, which will be subjected to strongly-coupled thermal (T), hydrodynamic (H), mechanical (M) and geochemical (C) processes. Here we present coupled THCM numerical simulations of laboratory and in situ tests performed with compacted FEBEX bentonite having different space and time scales. The simulations of the heating and hydration tests reproduce the measured temperature, water content and water intake data and the trends of the geochemical data. Although simulation results of the tests display similar trends, they show differences due to geometry, initial and confining conditions. The changes in porosity due to mineral dissolution/precipitation are not relevant in these tests, but become relevant in long-term simulations, which show that the precipitation of corrosion products reduces significantly the porosity of the bentonite near the canister and causes pore clogging. The thickness of the bentonite alteration band is simulated to be smaller than 7 cm after 1 Ma.

Keywords: Environmental engineering, Geochemistry, Radioactive waste disposal

List of notation

Equations and tables of parameter values are listed in Appendices 1 and 2

1. Introduction

The disposal of spent fuel and high-level radioactive waste (HLW) in deep geological repositories is based on a multibarrier concept, which includes the host rock (granite and clay) and the engineered barrier system (EBS). The EBS includes the waste form, the canister and the bentonite buffer. The geochemical evolution of the bentonite barrier depends on its porewater chemical composition, the temperature field, the hydration rate and the geochemical alteration processes at the interfaces of the bentonite and other materials such as the metallic canister, the concrete liner and the rock (Mon et al., 2017). A wide range of laboratory and in situ tests have been performed in the last decades to demonstrate the technical feasibility of the EBS, characterize the key processes and measure the key parameters of the bentonite (ENRESA, 2000a; Karnland et al., 2000; ENRESA, 2006a, 2006b; Verstricht et al., 2007; Olsson and Karnland, 2011). Numerical models have been performed to interpret these tests, characterize the couplings among thermal, hydraulic, chemical and mechanical processes and evaluate the long-term (>10,000 y) evolution of the EBS (Bildstein et al., 2006; Wersin et al., 2007; Samper et al., 2008c; Yang et al., 2008; Savage et al., 2010; Marty et al., 2010; Lu et al., 2011, Savage, 2012; Ngo et al., 2014, Samper et al., 2017, Mon et al., 2017).

Compacted bentonite exhibits a complex porosity structure with interlayer (2–10 Å), intraaggregate (micropores 50 Å) and interaggregate (macropores: 50–200 Å) pores (Bradbury and Baeyens, 2003; Fernández et al., 2004). The two dominant pore sizes in compacted bentonite are related to: 1) The macrostructure, associated with the global arrangements of clay aggregates (the skeleton) with macropores between them and 2) The microstructure, the active clay minerals and their vicinity (also called interlayer porosity) (Sánchez et al, 2012a). This double structure in FEBEX compacted bentonite has been detected in laboratory tests (Lloret et al., 2003, Villar et al., 2004) and has been simulated with THM (Sánchez et al., 2016b) and THC models (Zheng and Samper, 2015). The microporosity is always saturated and hydration and dehydration processes change the interlayer distance between clay platelets by adding or removing water molecules. The macroporosity is a multi-phase system, which contains water and vapor (Sedighi and Thomas, 2014). Dual porosity models have been used in soils to account for macropores (or

interaggregate pores) and intraaggregate pores. The double structure of bentonite not only affects its hydrodynamic behaviour, but also the chemical evolution (Samper et al., 2008b).

Solute diffusion in bentonite can take place through: 1) The interlayer water that forms part of the mineral structure; 2) The diffuse double layer (DDL) water that is present at the interface with the mineral surface and has an excess of cations and; 3) The free porewater, which is an electrically balanced solution. The diffusion coefficients are different in these domains. Appelo (2013) presented a compilation of the porosity and diffusion of the bentonite and provided evidences and explanations for the different behaviour of cations and anions. Ochs et al. (2001) reported a bentonite porosity model with free porewater and DDL water. Other models subdivide the effective diffusion coefficient in its components associated with free porewater, DDL water (known as surface diffusion), and interlayer water (Bourg et al. 2006, 2007). Leroy et al. (2006) developed a model for Cl^- in which the concentration in DDL water is calculated by Donnan equilibrium. This model explains the observed trends of larger and smaller diffusion coefficient for cations and anions, respectively. Gimmi and Alt-Epping (2018) and Alt-Epping et al. (2018) presented a simplified method to account for Donnan equilibria, which considers charged clay surfaces as immobile anions in the pore solution and uses the Nernst-Planck (NP) equation to simulate the coupled reactive transport. Tournassat and Appelo (2011) analyzed the structure of montmorillonite, estimated the volume of the interlayer porosity and its contribution to the water-filled porosity, and quantified anion exclusion. Alt-Epping et al. (2015) presented a benchmark problem for reactive transport to investigate the role of Fickian versus Nernst-Planck representations of diffusion. They conclude that the differences in concentrations differences are less than 8 %. Zheng and Samper (2015) proposed a dual continuum model (DCM) of non-isothermal multiphase flow and reactive transport with a *n*th-order solute transfer term, which extends the single porosity model reported by Samper et al (2008b). This model outperforms the single continuum model and confirms that solute transfer between the macro- and the micropore domains controls the long tails of the breakthrough curves.

FEBEX (Full-scale Engineered Barrier Experiment) was a demonstration and research project dealing with the EBS of a HLW repository in crystalline rock (ENRESA, 2000a; 2006a). The FEBEX project included a wide range of small-scale laboratory tests and two large-scale tests: (1) The mock-up test operated at the CIEMAT facilities in Spain (ENRESA, 2006a, Martín and

Barcala, 2005; Martín et al., 2006); and (2) The in situ test performed at the Grimsel underground research laboratory (URL) in Switzerland (ENRESA, 2000a; 2006a; 2006b). Laboratory tests were carried out on unsaturated bentonite samples with different sizes (13, 40 and 60 cm long column tests), durations and heating and hydration conditions (ENRESA, 2006a). Villar et al. (2008, 2008b) and Fernández and Villar (2010) reported the results of a series of laboratory heating and hydration tests (HHT) performed on 60 cm-long samples of compacted FEBEX bentonite with durations ranging from 0.5 to 7.6 years. These tests are the so-called CG column HHT. Villar et al. (2012) presented a summary of the information gathered during 15 years on the saturation of compacted FEBEX bentonite obtained from 40 cm-long HHT, the mock-up and the in situ tests. They analyzed the hydration rates, the temperature and the water content data and their relevance for vapor migration through the bentonite and bentonite saturation. Guimarães et al. (2007) and Zheng et al. (2010) presented fully coupled THCM models of the 13 cm-long HHT performed on samples of compacted FEBEX bentonite. These models accounted for cation exchange reactions and the dissolution/precipitation of carbonates, sulfates, halite and chalcedony. The model of Zheng et al. (2010) considered also surface complexation reactions. Zheng et al. (2010) concluded that: 1) Thermal osmosis is relevant for the hydration of FEBEX bentonite, 2) Chemical osmosis can be safely neglected, and 3) pH is mostly buffered by protonation/deprotonation via surface complexation. Villar et al. (2008b) presented a THM model of the CG column HHT and a comparison of measured and computed water intake, temperature, water content and porosity. Model results reproduced the general trends of the measured data. Sedighi et al. (2018) presented a coupled THC model of the CG column HHT, which accounts for the evolution of the microstructure. They concluded that the distribution of anionic species is controlled by the accessory minerals of the FEBEX bentonite such as carbonates and gypsum. Arcos et al. (2008) reported also the relevance of the accessory FEBEX bentonite minerals to buffer both pH and Eh. Sánchez et al. (2016a) analysed the relevance of thermo-osmotic flow for the heating and hydration of the bentonite barrier by comparing the numerical results with and without the thermos-osmosis process in the numerical simulations of the 40 cm-long tests and the HLW repository in granite. They concluded that the thermo-osmotic flow could be relevant for the long-term hydration of the HLW repository barrier and could explain the apparent low hydration rate observed in the 40 cm-long HHT. Sánchez et al. (2016b) presented THM

simulations of unsaturated expansive clays with a double-porosity formulation and concluded that the double-porosity formulation simulates more than one swelling stage, explains the observed kinetic swelling and reproduces the measured hydration rate of the HHT.

Sánchez et al. (2012a) reported a THM analysis of the FEBEX mock-up test with single and double porosity structures. The numerical simulations with the double porosity formulation reproduced well the experimental results. Zheng and Samper (2008) presented a coupled THMC analysis of the FEBEX mock-up test, which accounts for thermal and chemical osmosis and bentonite swelling with a state-surface approach.

The numerical simulations of the FEBEX in situ test are more complex than those of the FEBEX mock-up test because the hydration rate of the bentonite buffer in the in situ test is less controlled than in the mock-up test. Sánchez et al. (2012b) presented THM simulations of the FEBEX in situ test, which reproduce the measured water content and temperature data and predict that the bentonite barrier would become fully saturated after 20 years. Their simulations, however, showed limitations to reproduce the measured stress field. Samper et al. (2008a) presented a coupled THC model of the FEBEX in situ test, which achieved a good fit to measured temperature data and reproduced the general trends of the measured dissolved concentrations. The THC model, however, did not reproduce the water content and dry density data because this model failed to account for bentonite swelling. This limitation was overcome by Zheng et al. (2011) and Samper et al. (2018), who reported a coupled THCM model of the FEBEX in situ test, which accounts for bentonite swelling and thermal and chemical osmosis. Zheng et al. (2015, 2017) presented coupled THMC models of Kunigel-VI and FEBEX bentonites to evaluate the relevance of bentonite illitization and other chemical changes in the EBS and their effect on the mechanical propertied of the EBS for temperatures above 100°C.

The models developed within the context of the FEBEX project were used by Samper et al. (2008c), Lu et al. (2011) and Samper et al. (2016) to evaluate the long-term (1 Ma) hydrogeochemical evolution of the EBS of a repository in granite and by Yang et al. (2008) and Mon et al. (2017) to evaluate the evolution of a repository in clay.

Here we present coupled THCM numerical simulations of the EBS. These simulations include: 1) The models of the CG column HHT, the mock-up and the in situ tests; and 2) The long-term (1 Ma) geochemical simulations of the EBS. The paper starts with the description of the FEBEX

tests. Then, the conceptual and numerical THCM models of the tests are presented. Afterwards, the long-term (1 Ma) simulations of the geochemical evolution of the EBS of a repository in granite are described. The paper ends with the main conclusions.

2. FEBEX in situ and lab tests

The Spanish Reference Concept of a high-level radioactive (HLW) waste repository in granite envisages the emplacement of the waste in cylindrical carbon steel canisters with 0.9 m diameter. The canisters are laid in deep horizontal galleries and embedded into a 0.75 m thick bentonite buffer (ENRESA, 2000b) (Figure 1). The FEBEX mock-up and in situ tests replicate the concept of the repository except that the canisters containing the spent fuel were replaced by two heaters. Both tests started in February of 1997. The FEBEX in situ full-scale test was performed at the Grimsel underground research laboratory (URL) in Switzerland (ENRESA, 2000a; 2006a). The test included the heating system, the clay barrier and the instrumentation, monitoring and control system. The drift was 70.4 m long and 2.27 m in diameter (ENRESA, 2006a). The test zone was located in the last 17.4 m of the drift where two heaters, the bentonite barrier and the instrumentation were installed (Fig. 1). The heaters were placed inside a cylindrical steel liner having a diameter of 0.93 m, which had been installed concentrically with the drift. The heaters maintained a maximum temperature of 100 °C at the liner/bentonite interface. The bentonite barrier was made of blocks of highly-compacted bentonite. The test was performed in two operational periods (ENRESA, 2000a; 2006a; 2006b). The 1st period lasted from 1997 to 2002 when heater 1 was switched off and the area around it was dismantled. Heater 2 was turned off and the full test was dismantled in 2015 (Kaufhold S et al., 2018; Carbonel et al., 2019; García-Siñeriz et al., 2019; Villar et al., 2018; 2019) (Figure 1). The components of the FEBEX mock-up test are similar to those of the in situ test: two electric heaters, a 0.64 m-thick clay barrier, the instrumentation, and data acquisition system. The bentonite buffer is confined in a steel structure, which ensures a uniform temperature and water pressure around the external surface of the buffer (Figure 1). The clay barrier is made of compacted bentonite blocks of dry density of 1.7 g/cm^3 (Martín and Barcala, 2005; Martín et al., 2006).

The so-called CG column heating and hydration tests were performed on cylindrical samples (60 cm long and 7 cm in diameter) of compacted FEBEX bentonite (Figure 1) (Villar et al., 2008a; 2008b). The duration of the CG column HHT ranged from 0.5 to 7.6 years. Sample columns were

prepared with FEBEX bentonite blocks compacted to a dry density of 1.65 g/cm^3 with an initial water content of 14% (ENRESA 2000, 2006a). The bentonite samples were installed in a Teflon cover to reduce lateral heat dissipation and bentonite deformation. The hydration system maintained a water pressure of 1.2 MPa at the top of the cells. Heaters were installed at the bottom of the cells to maintain the temperature at 100ºC (Figure 1). The main features of the FEBEX in situ, mock-up and CG column HHT are listed in Table 1.

Table 1. Summary of the main features of the numerical models of the FEBEX heating and hydration tests in the 60 cm-long CG column HHT (Mon, 2017), the mock-up test (Zheng and Samper, 2008) and the in situ test (Samper et al., 2008a; Zheng et al., 2011; Samper et al., 2018) and the long-term predictions of the geochemical evolution of a HLW repository (Samper et al., 2008c; Lu et al., 2011; Samper et al., 2016). 1DP = 1D Parallel. 2DA = 2D Axisymmetric.

Test	Time horizon (days)	Bentonite thickness (m)	Cumulative water intake (L)	Initial volumetric water content	Heater/canister temperature (ºC)	Model results				
						Cumulative water intake	Water content	Temperature	Solute concentrations	Flow configuration
CG column HHT	188-440	0.60	0.17-0.46	0.223	100	Yes	Yes	Yes	Yes	1D-P
Mock-up test	7300	0.62	1120	0.351	100	Yes	Yes	Yes	No	2D-A
In situ test	6786	0.66	-	0.245	97	No	Yes	Yes	Yes	2D-A
HLW repository	$3.65 \cdot 10^8$	0.75	-	0.407	97-30	No	No	Yes	Yes	2D-A

3. THCM conceptual model of the FEBEX heating and hydration tests

The CG column HHT and the mock-up and the in situ tests show differences in geometry, dimensions, durations and initial conditions (Table 1). It should be noticed that water flow and heat transfer in the bentonite columns of the 60 cm-long cells is 1-D parallel with water flowing from the hydration side to the column end at the heater. On the other hand, the mock-up and the in situ tests have a cylindrical configuration. Water flow and heat transfer in these tests is 2-D axisymmetric (Figure 2). The bentonite barrier is hydrated from the external cylindrical surface and water flows towards the internal heater/bentonite interface (Villar et al., 2012; Mon, 2017).

3.1 Thermo-hydro-mechanical processes

The bentonite barrier is initially unsaturated, and it progressively hydrates from the surrounding rock towards the canister. The water content of the bentonite in these HHT increases near the hydration boundary. Bentonite hydration leads to bentonite swelling. Therefore, the porosity of the bentonite increases during bentonite hydration.

Here, we consider a single porosity medium and a simplified approach for bentonite swelling, which is described by a state surface relating void ratio to the effective stress, suction and air pressure (see Eq. 25 of the Appendix 1). Mechanical and swelling processes play an important role in the hydrodynamic and geochemical evolution of the EBS during the early heating and hydration stage of the EBS, when bentonite buffer is subjected simultaneous to heating and hydration.

The temperature is fixed at 100ºC on the heater/bentonite interface. Water evaporates near the heater. Vapor diffuses away from the heater and condenses in cooler places. Vapor condensation retards the hydration of the bentonite buffer and affects the concentration of the dissolved species (Zheng et al, 2011; Villar et al., 2012).

The conditions of the FEBEX HHT call for a coupled non-isothermal multiphase flow conceptual model with: 1) Advection of water in the liquid phase; 2) Advection and diffusion of vapor in the gaseous phase; 3) Advection and diffusion of air in the liquid and gaseous phases; 4) Convection of heat in the liquid and gaseous phase and; 5) Heat conduction. The unsaturated bentonite swells under non-isothermal conditions when it is hydrated. Therefore, a coupled THM formulation is required for these tests. The THM mathematical formulation is presented in Appendix 1.

3.2 Solute transport and geochemical reactions

Solute transport processes include: advection, molecular diffusion and mechanical dispersion. The following chemical reactions take place at the EBS: aqueous complexation, acid-base, redox, mineral dissolution/precipitation, cation exchange and proton surface complexation. The geochemical system is defined in terms of the following primary species: H_2O, H^+, Ca^{2+}, Mg^{2+}, Na^+, K^+, Cl^-, SO_4^{2-}, HCO_3^- and $SiO_2(aq)$. The bentonite contains initially calcite, silica minerals and gypsum. These minerals can be safely assumed at local chemical equilibrium. Anhydrite may precipitate at temperatures above 50ºC. Smectite dissolution is very slow and not relevant in the HHT, although it can be relevant for the long-term evolution of the EBS. The relevant aqueous complexes are commonly identified with chemical speciation codes such as EQ3NR (Wolery,

1992). Cation exchange reactions of dissolved Na^+, K^+, Ca^{2+} and Mg^{2+} are modelled with the Gaines-Thomas convention. The cation exchange capacity of the FEBEX bentonite is equal to 102 meq/100g (Fernández et al., 2004). Surface complexation reactions are modelled with the triple sorption-sites model of Bradbury and Baeyens (1997; 2003). The equilibrium constants of the aqueous complexation, mineral dissolution/precipitation, surface complexation and cation exchange reactions at 25ºC are listed in Table 2 of Appendix 2. The mathematical formulation of solute transport processes and geochemical reactions is presented in Appendix 1.

4. Numerical implementation and computer codes

The numerical models of the CG column HHT and the mock-up and the in situ tests were performed with INVERSE-FADES-CORE V2 (Zheng and Samper, 2004, 2005), a THMC code, which solves both forward and inverse non-isothermal multiphase flow and multicomponent reactive transport problems in 1-, 2- and 3-D axisymmetric porous and fractured deformable media. This code integrates the capabilities of FADES (Navarro, 1997), a THM code, CORE^{2D} (Samper et al., 2009), FADES-CORE (ENRESA 2000b) and INVERSE-CORE (Dai and Samper, 2004). State variables of the forward model include liquid and gas pressures, temperature, solid displacements and the concentrations of the primary aqueous species, the exchanged cations and the mineral phases.. The discretized equations are solved with an iterative Newton–Raphson method. The coupled solute transport and chemical equations are solved with a sequential iteration method.

The numerical model of the long-term geochemical evolution of the EBS was performed with CORE^{2D} V4 (Samper et al., 2003; 2009), a code for transient saturated and unsaturated water flow, heat transport and multicomponent reactive solute transport under both local chemical equilibrium and kinetic conditions in heterogeneous and anisotropic media. The code has been used to model laboratory and in situ tests (Soler et al., 2008; Samper et al., 2008b,c; 2016).

5. Numerical models of HHT

Although the conceptual THCM model of the HHT is the same for the CG column HHT and the mock-up and in situ tests, there are differences in the numerical models of these tests due to differences in the geometry, duration, initial and boundary conditions (see Table 1). Figure 2 shows the schemes of the numerical models of the CG column HHT and the mock and in situ tests.

The hydrodynamic parameters of the THMC models of the HHT are listed in Table 3 of Appendix 2. According to ENRESA (2006a) and Zheng and Samper (2008), bentonite hydration is mostly sensitive to the liquid intrinsic permeability, the vapor tortuosity factor and the thermo-osmotic permeability. The intrinsic permeability of the liquid was measured in laboratory tests (ENRESA, 2006a; Villar et al., 2018). The intrinsic permeability for the CG column HHT, the mock-up test and in situ test were calibrated using measured water intake data and are equal to $2.75 \cdot 10^{-21}$, $3.5 \cdot 10^{-21}$ and $3.75 \cdot 10^{-21}$ m^2, respectively. These values are within the 30% range of variation of the experimental values (Villar et al., 2018). The relative permeability of the liquid and the gas and the thermo-osmotic permeability were taken from Zheng and Samper (2008) and Zheng et al. (2010). The vapor tortuosity factor is used to calculate the vapor diffusion coefficient and takes values from 0 to 1. The vapor tortuosity factor was calibrated to reproduce the measured relative humidity data, especially near the heater. The vapor tortuosity factors of the CG column HHT, the mock-up test and in situ test are equal to 0.4, 0.09 and 0.2. The differences in the tortuosity are related to differences in the gaps between the bentonite blocks.

The thermal and mechanical parameters of the THMC models of the HHT are listed in Tables 4 and 5 of Appendix 2, respectively.

The solute transport parameters of the bentonite are listed in Table 6 of Appendix 2, respectively. The molecular diffusion in water, D_o, is the same for all the aqueous species for the CG column HHT and mock-up test and equal to $2 \cdot 10^{-10}$ m^2/s, except for Cl^- for which the diffusion coefficient is $9 \cdot 10^{-11}$ m^2/s based on the model of the 13 cm-long HHT (Zheng et al., 2010). For the in situ test, the diffusion coefficients of Cl^- and SO_4^{2-} were taken from García-Gutiérrez et al. (2004) and (2006). The diffusion in water is equal to $3 \cdot 10^{-12}$ m^2/s for Cl^-, $3.6 \cdot 10^{-13}$ m^2/s for SO_4^{2-} and $2 \cdot 10^{-11}$ m^2/s for the rest of the chemical species.

The initial concentrations of the primary species of the bentonite pore water were taken from Fernández et al. (2001). The hydration waters in these tests were granitic waters (see Table 7 in Appendix 2). It should be noticed that the concentrations of the solutes in the bentonite are larger than those of the hydration waters (Table 7).

Table 8 presents the initial mineral volume fractions, the initial concentrations of exchanged cations and the total concentrations of surface complexation sites considered in the HHT.

5.1 CG column HHT

304 The numerical model of the CG column HHT was performed with a 1-D finite element mesh (Mon,
305 2017). Model results were computed for the durations of the tests: 0.5 (CG0.5 and CG0.5b), 1
306 (CG1 and CG1b), 2 (CG2 and CG2b) and 7.6 years (CG7.6). The proper simulation of the pH and
307 the sulfate minerals requires that the numerical model accounts for the heating and hydration
308 stage as well as for the cooling phase of 2 days to take into consideration the effect of mineral
309 dissolution/precipitation during the dismantling, the sample gathering and the laboratory analysis.
310 The bentonite sample had initially a porosity of 0.4 and a gravimetric water content of 14%, which
311 corresponds to a water saturation of 57% and a suction of $1.27 \cdot 10^5$ kPa. The initial temperature
312 was equal to 22ºC and the initial gas pressure was equal to the atmospheric pressure. The liquid
313 pressure was fixed at 1200 kPa at the hydration boundary. The temperature at the heater was
314 prescribed at 100ºC.
315 The CG column HHT were performed by allowing an increase in the size of the bentonite
316 sample due to the displacement of the bentonite sample and the change in bentonite
317 porosity. The volumetric deformation was simulated by allowing the displacement of the
318 nodes of the finite element grid. Only the node at hydration boundary was fixed by
319 prescribing a zero displacement.
320 The heater boundary is closed for liquid and gas flow. A thermal Cauchy condition was used to
321 account in an approximate manner for the lateral heat dissipation through the Teflon wall cell
322 (Fernández and Villar, 2010). The thermal Cauchy coefficient was taken equal to 1000 W/ºC. A
323 Neuman boundary condition was used for solute transport at the hydration boundary according
324 to which the solute flux was equal to the product of the water flux times the solute concentration
325 of the inflow water.
326 ***5.2 FEBEX mock-up and in situ tests***
327 The models of the mock-up test (Zheng and Samper, 2008) and the in situ test (Samper et al.,
328 2008a; Zheng et al., 2011; Samper et al., 2018) were performed with a 1-D axisymmetric mesh
329 (Figure 2). The model parameters and the boundary conditions of these tests are similar to those
330 of the 60 cm-long column tests, except for the prescribed liquid pressures at the hydration
331 boundary which were equal to 550 kPa and 700 kPa for the mock-up and the in situ tests,
332 respectively.

6. Models results of HHT

6.1 THM results

The computed water intake increases with time as the bentonite barrier is hydrated. Figure 3 shows the comparison of the computed water intake and the measured data for the CG column HHT of 7.6 years (CG7.6) and the mock-up test. The slope of the water intake curve is large at early times. Later, it decreases noticeably. Bentonite hydration in the mock-up test is faster than that in the CG7.6 column HHT due to the initial flooding of the mock-up test and also due to the differences in geometric configuration (axisymmetric versus parallel flow) (Mon, 2017). The computed water intake values for the CG7.6 column HHT coincide with those reported by Villar et al. (2008b). Similarly, the calculated water intake values for the mock-test reproduce the measured values.

The radial distributions of the computed gravimetric water content and the porosity show the swelling of bentonite near the hydration boundary and bentonite shrinkage near the heater. The gravimetric water content and the porosity increase from the initial values near the hydration boundary and decrease near the heater (Figure 4). The computed values reproduce the general trends of the measured data. The computed water content and porosity of the mock-up and in situ tests show similarities. The computed water content and the porosity in the CG column HHT near the hydration boundary, however, are slightly smaller than those of the mock-up and in situ tests because the flow in the CG column HHT is 1D parallel and the flow in the mock-up and in situ tests is 1D axisymmetric. It should be pointed out that the computed water contents are similar to those reported by Villar et al. (2008b). The computed water saturation degree show that the bentonite reaches almost full saturation near the hydration boundary while the bentonite dries out near the heater where the saturation degree is smaller than the initial saturation. The computed temperatures reach steady state after a few days. The temperature is largest at the heater and smallest at the hydration boundary. Failing to account for the mechanical component of the THCM model leads to model deviations from experimental data. Figure 3 shows the computed cumulative water intake for the CG column HHT of 7.6 years with and without bentonite swelling. The water intake and the gravimetric water content of the bentonite are grossly underestimated when bentonite swelling is not taken into account (Figures 3 and 4). Model deviations in water

intake and water content have also a significant impact in the computed solute concentrations (Figure 5).

6.2 Chemical results

Advection is the main solute transport mechanism during the early stages of the bentonite hydration (Zheng et al, 2011). The advective flux in the bentonite decreases upstream of the wetting front because the hydraulic gradient decreases extremely when the liquid saturation degree increases. Solute dispersion is due to the combined effect of molecular diffusion and hydrodynamic dispersion. The water velocity is large during the early stages of the bentonite hydration. Later, however, it decreases exponentially. Therefore, the dispersive term decreases with time and becomes negligible compared to molecular diffusion after about 3 days in the CG column HHT and 15 days in the mock-up and in situ tests (Samper et al., 2018).

The spatial distribution of the dissolved concentration of a conservative species such as Cl^- depends on the inward displacement of the hydration front, the water evaporation at the heater/bentonite interface, the condensation of vapor some cm away from the heater, and the advective and dispersive transport of dissolved Cl^- in the bentonite. The concentration of dissolved Cl^- decreases near the hydration boundary due to dilution with the hydration water while it increases near the heater due to the water evaporation.

Figure 5 shows the spatial distribution of the computed and measured concentrations of dissolved Cl^- in the CG column HHT and the in situ test at selected times. The computed concentrations of Cl^- show dilution fronts which move away from the hydration boundaries. These fronts were also reported by Sedighi et al. (2018). In addition, the computed concentrations of dissolved Cl^- near the heater are higher than the initial concentration due to the evaporation of the bentonite pore water. Our computed concentrations of Cl^- show similar trends to those reported by Sedighi et al. (2018), except for the CG7.6 column HHT. Our computed Cl^- concentration near the heater underestimate the measured data, probably due to the uncertainties in the effective diffusion coefficient of Cl^- in dry conditions. Other dissolved species show similar patterns to those of Cl^-, but they are also affected by cation exchange and mineral precipitation/dissolution reactions. The computed concentrations of the dissolved species in the CG column HHT are consistent with the laboratory observations reported by Fernández and Villar (2010) and with the computed values of Sedighi et al. (2018).

392 A calcite dissolution/precipitation front moves in the bentonite from the hydration boundary. This
393 front is induced by the inflow of the hydration water. Calcite is expected to precipitate near the
394 heater due to water evaporation and the decrease of calcite solubility with temperature. The
395 computed concentrations of dissolved/precipitated calcite in the CG7.6 column HHT show a thin
396 band near the heater where calcite dissolves due to the precipitation of anhydrite (Figure 6). This
397 result is also shown at the end of the in situ test (Figure 6).
398 Model results for gypsum dissolution/precipitation for the CG column HHT and the in situ tests
399 show similar trends (Figure 7). A small amount of gypsum dissolves initially in the bentonite in the
400 in situ test because the initial bentonite pore water is not at equilibrium with this mineral. This
401 mineral remains inactive during the heating stages of the experiment. Gypsum precipitates near
402 the heater after the cooling period (Figure 7). The computed concentrations of gypsum in the CG
403 column HHT show a dissolution front in the bentonite, which moves away from the hydration
404 boundary. All the gypsum initially present in the CG column HHT is dissolved in the 12 cm closest
405 to the hydration boundary. Sedighi et al. (2018) also reported a similar result. Gypsum precipitates
406 during the cooling phase near the heater (in the interval 0.5 m < x < 0.6 m) in the CG column
407 HHT. Gypsum precipitates also near the heater in the in situ test after 5 and 18 years. Gypsum
408 precipitation in the in situ test is smaller than that in the CG column HHT.
409 Anhydrite is a mineral that is not initially present in the bentonite. It precipitates near the heater
410 because the solubility of anhydrite is smaller than that of gypsum for temperatures above a
411 threshold temperature ranging from 43º to 56º C. Most of the precipitated anhydrite transforms
412 into gypsum after switching off the heater. This transformation is assumed to occur sufficiently
413 fast. Some anhydrite remains precipitated near the heater in a thin band of a few mm (Figure 8).
414 Sedighi et al. (2018) also reported a significant amount of anhydrite precipitation near the heater.
415 The initial pH in the bentonite is 7.72. The pH of the bentonite pore water is controlled by the
416 temperature field and by surface protonation and calcite dissolution/precipitation reactions. In
417 general, the pH decreases near the hydration boundary due to the calcite dissolution/precipitation
418 front and increases near the heater due to calcite precipitation (Figure 9).
419 The changes in porosity due to mineral dissolution/precipitation reactions are not relevant for the
420 short-term HHT. However, these changes become relevant in the long-term evolution (see the
421 next section).

7. Long-term evolution of the EBS

7.1 Conceptual and numerical model

The safety assessment of a HLW geological repository requires the simulation of the long-term evolution of the EBS. The bentonite barrier becomes nearly saturated after a few decades (Zheng and Samper, 2008). The water flow and the bentonite swelling become negligible when the EBS is saturated. The thermal gradients in the EBS last for thousands of years and influence the geochemical evolution of the bentonite. Solute diffusion becomes the main solute transport process because the hydraulic conductivity of the bentonite is extremely low ($6 \cdot 10^{-14}$ m/s). Canister corrosion and the chemical interactions of corrosion products and bentonite are the key geochemical processes (Samper et al., 2008c; Savage, 2010; Marty et al., 2010; Lu et al., 2012; Ngo et al., 2014; Samper et al., 2016).

The long-term simulation of the geochemical evolution of the EBS has been performed with a 1-D axisymmetric model (Figure 2) for a time horizon of 1 Ma (Samper et al., 2008c; Lu et al., 2011; Samper et al, 2016). The geometry is based on the Spanish Reference Concept for a HLW repository in granite (ENRESA, 2000b). The long-term simulation of the EBS starts once the bentonite barriers is saturated. A non-isothermal multicomponent reactive transport model (THC) is used. Mechanical processes are disregarded. Although the mechanical processes are negligible for the long-term simulation of the EBS, accounting for them in short term simulations is essential to establish a realistic initial bentonite pore water composition for the long-term simulations.

The effective diffusion coefficient, D_e, was equal to $4.07 \cdot 10^{-11}$ m^2/s for all the aqueous species. The bentonite porosity is equal to 0.407. The flushing effect of granitic groundwater flow has been simulated by imposing near the bentonite-granite interface an inflow of 0.1 L/y of granitic groundwater and an outflow of 0.1 L/y of bentonite porewater (Figure 2). The geochemical model for the long-term simulations accounts for anoxic canister corrosion, surface complexation of Fe^{2+} and cation exchange of Fe^{2+} besides the chemical reactions considered for the short-term HHT (see Tables 2 and 9).

The time evolution of temperature is prescribed at the canister/bentonite interface according to the long-term thermal simulations of ENRESA (2000b). The initial temperature is equal to 30 ºC, the estimated natural temperature of the rock at the depth of the repository. At the

canister/bentonite interface, the temperature reaches a maximum of 97 ºC after 24 years. Then, it decreases smoothly. At the bentonite/granite interface, the temperature reaches 78ºC after 100 years. The thermal parameters were taken from ENRESA (2000a). The heat transport through the bentonite buffer is solved and the computed temperatures are used to update the chemical and transport temperature-dependent parameters. The model accounts for the dependence of the corrosion rate on temperature with an activation energy equal to 11 kJ/mol (Feron et al., 2008). The chemical compositions of the granite porewater and the initial bentonite porewater are listed in Table 10.

7.2. Model predictions

The canister corrosion rate increases from its initial value equal to 2 μm/y to 4.75 μm/y and then decreases smoothly due to the change in temperature (Figure 10). The canister is fully corroded after $3 \cdot 10^4$ years. Canister corrosion leads to a rise of pH, which reaches nearly 9.5 at $2 \cdot 10^5$ years, and the concentration of dissolved Fe^{2+} of bentonite porewater. Most of the released Fe^{2+} precipitates as magnetite and siderite or sorbs via cation exchange and surface complexation on weak sites. The computed pH, Eh and the concentration of dissolved Fe^{2+} show fronts related to surface complexation reactions in the bentonite. The precipitation of corrosion products progresses as dissolved Fe^{2+} diffuses through the bentonite and reduces significantly the porosity of the bentonite near the canister. Magnetite is the main corrosion product (Figure 10). Siderite precipitation after 1 Ma at the canister-bentonite interface (<2.5 mol/L) is much smaller than magnetite precipitation (~70 mol/L). Goethite does not precipitate. The thickness of bentonite affected by the porosity decrease is smaller than 7 cm after 1 Ma. The changes in porosity due to chemical reactions in the rest of the bentonite buffer are negligible. More details on the changes in porosity are given by Samper et al. (2016).

8. Discussion and relevance of the simulations

Non-isothermal unsaturated conditions prevail in the early stages of the EBS. Bentonite swells during hydration while water evaporates near the heater. Therefore, coupled THMC models to simulate the early stages of the EBS evolution. Laboratory and in situ tests have been performed to identify the key processes and estimate the EBS parameters. These tests have been simulated with THM, THC and THMC models. The simulation results of the laboratory and in situ HHT show for the most part similar trends. However, there are differences that can be attributed to

differences in: 1) The geometric configuration (parallel versus axisymmetric flow), 2) The initial conditions; 3) The confining conditions; and 4) The dry density and the temperature inside the bentonite. The integrated analysis of the measured data and the simulation results of the FEBEX HHT has been most useful to gained insight into the coupled THMC processes of the EBS. Bentonite swelling plays a very important role in the hydrodynamic and geochemical evolution of the EBS during the early hydration stage when the bentonite buffer is subjected simultaneously to heating and hydration. Failing to account for the mechanical component of the THCM model leads to model deviations from measured data. The coupled THMC models of the HHT have been useful to: 1) Provide the thermal and geochemical model for the long-term predictions; 1) Provide the initial conditions for the long-term simulations, and 3) Gain confidence in the predictive capabilities of the THCM models.

9. Conclusions

Coupled THCM numerical simulations of the engineered barrier system (EBS) of a HLW repository have been presented. Simulations have been carried out for lab and in situ HHT performed with compacted FEBEX bentonite. Model results for the CG column HHT and the in situ test show similar trends. The hydration rate of the bentonite is large at early times, but later slows down significantly. The gravimetric water content and the porosity near the hydration boundary increase due to the bentonite hydration and swelling. On the other hand, the gravimetric water content near the heater decreases with respect to its initial value due to water evaporation. The concentration of dissolved Cl^- near the hydration boundary decreases due to the dilution with the hydration water, in which the solute concentrations are smaller than those of the bentonite porewater. The concentration of dissolved Cl^- is largest near the heater due to water evaporation. The hydration water triggers calcite dissolution and gives place to a dissolution/precipitation, which moves behind the hydration front. Calcite dissolves upstream the front while it precipitates downstream the front. Anhydrite precipitates at the bentonite/heater interface. The depletion of dissolved Ca^{2+} leads to calcite dissolution and the release of exchanged Ca^{2+}. The pH is buffered by calcite dissolution/precipitation and especially by surface protonation reactions.

Long-term simulations of the EBS have been used to assess the potential alterations of the EBS which could compromise its long-term stability. Once the bentonite barrier is almost saturated, water flow and bentonite swelling become negligible. The chemical interactions of canister

corrosion products and bentonite become the main processes for the long-term EBS alteration. Canister corrosion rises the pH and releases Fe^{2+}, which precipitates mainly as magnetite. A small fraction of the released Fe^{2+} sorbs via cation exchange and surface complexation. The precipitation of corrosion products reduces significantly the porosity of the bentonite and causes pore clogging. The thickness of the bentonite alteration band is smaller than 7 cm after 1 Ma.

The model results could be improved by considering a more realistic mechanical model than the state-surface approach as proposed by Guimarães et al. (2007); Villar et al. (2008); Sánchez et al. (2012a; 2012b) and more complex porosity structures such as the dual continuum model of Sánchez et al. (2005; 2012a; 2016b) and the model of Sedighi et al. (2018), which accounts for the evolution of the microstructure.

Acknowledgements

The research leading to these results received funding from the PEBS Project of the European Atomic Energy Community's Seventh Framework Programme (FP7/2007-2011) under grant agreement 232598. This work was partly funded by ENRESA (Spain), the Spanish Ministry of Economy and Competitiveness and FEDER Funds (Project CGL2016 78281) and Galicia Regional Government (Fund ED431C 2017/67 from "Consolidación e estruturación de unidades de investigación competitivas", Grupos de referencia competitiva). Alba Mon enjoyed a research contract from University of A Coruña. We thank the comments and corrections of the two anonymous reviewers because they contributed to improve the manuscript.

References

Alt-Epping P, Tournassat C, Rasouli P, Steefel CI, Mayer KU, Jenni A, Mäder U, Sengor SS and Fernández R. (2015) Benchmark reactive transport simulations of a column experiment in compacted bentonite with multispecies diffusion and explicit treatment of electrostatic effects. Computational Geoscience 19: 535-550.

Alt-Epping P, Gimmi T, Wersin P and Jenni A (2018) Incorporating electrical double layers into reactive-transport simulations of processes in clays by using the Nernst-Planck equation: a benchmark revisited. Applied Geochemistry 89: 1–10.

Appelo CAJ (2013) A Review of Porosity and Diffusion in Bentonite. Working Report 2013-29, Possiva, Finland, 33 pp.Bildstein O, Trotignon L, Perronnet M and Jullien M (2006) Modelling iron-clay interactions in deep geological disposal. Physics and Chemistry of the Earth 31: 618-625.

Arcos D, Grandia F, Domènech C, Fernández A M, Villar M V, Muurinen A, Carlsson T, Sellin P and Hernán P (2008). Long-term geochemical evolution of the near field repository: Insights from reactive transport modelling and experimental evidences. Journal of Contaminant. Hydrology 102 (3-4): 196-209.

Bourg I C, Sposito G and Bourg ACM (2006) Tracer diffusion in compacted, water-saturated bentonite. Clay Minerals 54: 363–374.

Bourg IC, Sposito G and Bourg ACM (2007) Modeling cation diffusion in compacted water saturated sodium bentonite at low ionic strength. Environmental Science and Technology 41: 8118–8122.Bradbury M H and Baeyens B (1997) A mechanistic description of Ni and Zn sorption on Na-montmorillonite. Part II: modelling. Journal of Contaminant Hydrology 27:223–248.

Bradbury M H and Baeyens B (2003). Porewater chemistry in compacted resaturated MX-80 bentonite. Journal of Contaminant Hydrology 61: 329–338.

Dai Z and Samper J (2004) Inverse problem of multicomponent reactive chemical transport in porous media: formulation and applications. Water Resources Research 40: W07407.

ENRESA (2000a) FEBEX Project. Full-scale engineered barriers experiment for a deep geological repository for high-level radioactive waste in crystalline host rock. Technical Report. ENRESA 1/2000, Madrid, 354 pp.

ENRESA (2000b) Evaluación del comportamiento y de la seguridad de un almacenamiento de combustible gastado en una formación granítica. ENRESA Technical Report PT 49-IPP-M-15-01, 84 pp [in Spanish].

ENRESA (2006a) Full-Scale Engineered Barriers Experiment: Updated Final Report. ENRESA Technical Report PT 05-02/2006, 589 pp.

ENRESA (2006b) FEBEX: Final THG modelling report. ENRESA Technical Report PT 05-3/2006, 155 pp.

Fernández A M, Cuevas J and Rivas P (2001) Pore water chemistry of the FEBEX bentonite. Materials Research Society Proceedings 663: 573–588.

Fernández A M, Baeyens B, Bradbury M and Rivas P (2004) Analysis of the pore water chemical composition of a Spanish compacted bentonite used in an engineered barrier. Physics and Chemistry of the Earth 29 (1): 105–118.

Fernández A M and Villar M V (2010) Geochemical behavior of bentonite barrier in the laboratory after up to 8 years of heating and hydrating. Applied Geochemistry, 25: 809-824

Fernández A M, Sánchez-Ledesma D M, Melón A, Robredo L M, Rey J J, Labajo M, Clavero M A, Carretero S and González A E (2018) Thermo-hydro-geochemical behaviour of a Spanish bentonite after of the FEBEX in situ test at the Grimsel Test Site. In: Technical Report CIEMAT/DMA/2G216/03/16. Nagra Arbeitsbereicht NAB16-025. NAGRA (Madrid, 270 pp).

Feron D, Crusset D and Grass J M (2008) Corrosion issues in nuclear waste disposal. Journal of Nuclear Materials 379:16-23.

García-Gutiérrez M, Cormenzana J L, Missana T and Mingarro M (2004) Diffusion coefficients and accessible porosity for HTO and ^{36}Cl in compacted FEBEX bentonite. Applied Clay Science 26: 65–73.

García-Gutiérrez M, Cormenzana J L, Missana T, Mingarro M and Molinero J (2006) Overview of laboratory methods employed for obtaining diffusion coefficients in FEBEX compacted bentonite. Journal of Iberian Geology 32 (1): 37–53.

García-Siñériz J L., Rey M., Kober F. and Sakaki T. (2019) Performance of THM monitoring instrumentation in FEBEX bentonite barrier after 18 years of operation under repository-like conditions. Geomechanics for Energy and the Environment 17: 75–89.

Gimmi T and Alt-Epping (2018) Simulating Donnan equilibria based on the Nernst-Planck equation. Geochimica et Cosmochimica Acta 232:1–13.

Guimarães, L., Gens A. and Olivella S. (2007) Coupled thermo-hydro-mechanical and chemical analysis of expansive clay subjected to heating and hydration. Transport in Porous Media 66 (3): 341-372.

Karnland O, Sandén T, Johannesson L E, Eriksen T E, Janson M, Wold S, Pedersen K, Motamedi M and Rosborg B (2000) Long term test of buffer material. Final report on the pilot parcels. SKB Technical Report 00-22, 131 pp.

Kaufhold S, Dohrmann R, Ufer K and Kober F (2018) Interactions of bentonite with metal and concrete from the FEBEX experiment: mineralogical and geochemical investigations of selected sampling sites. Clay Minerals 53: 745–763.

Keijzer T J S, Kleingeld P J and Loch J P G (1999) Chemical osmosis in compacted clayey material and the prediction of water transport. Engineering Geology 53: 151–159.

Keijzer T J S and Loch J P G (2001) Chemical osmosis in compacted dredging sludge. Soil Science Society of American Journal 65: 1045–1055.

Leroy P, Revil A and Coelho D (2006) Diffusion of ionic species in bentonite. Journal of Colloid Interface Science 296: 248–255.

Lloret A and Alonso E E (1995) State surfaces for partially saturated soils. In: Proceedings of the International Conference on Soils Mechanics and Foundation Engineering, Balkema, pp. 557–562.

Lloret A, Villar MV, Sánchez M, Gens A, Pintado X and Alonso EE (2003). Mechanical behaviour of heavily compacted bentonite under high suction changes. Géotechnique 53(1):27–40.

Lu C, Samper J, Fritz B, Clement A and Montenegro L (2011). Interactions of corrosion products and bentonite: an extended multicomponent reactive transport model. Physics and Chemistry of the Earth 36, 1661-1668.

Marty N C M, Fritz B, Clément A and Michau N (2010) Modelling the long-term alteration of the engineered bentonite barrier in an underground radioactive waste repository. Applied Clay Science 47: 82-90.

Martín P L and Barcala J M (2005) Large scale buffer material test: mock-up experiment at Ciemat. Engineering Geology 81(3): 298-316.

621 Martín P L, Barcala J M and Huertas F (2006) Large-scale and long-term coupled thermo-hydro-
622 mechanic experiments with bentonite: the FEBEX mock up test. Journal of Iberian Geology 32
623 (2): 259-282.
624 Mon A (2017) Coupled Thermo-Hydro-Chemical-Mechanical Models for the Bentonite Barrier in
625 a Radioactive Waste Repository. Ph.D. Dissertation. University of A Coruña, Spain, 483 pp.
626 Mon A, Samper J, Montenegro L, Naves A and J Fernández (2017) Long-term nonisothermal
627 reactive transport model of compacted bentonite, concrete and corrosion products in a HLW
628 repository in clay, Journal of Contaminant Hydrology 197: 1-16.
629 Navarro V (1997) Modelo de comportamiento mecánico e hidráulico de suelos no saturados en
630 condiciones no isotermas. Ph.D. Dissertation, Universidad Politécnica de Cataluña, 329 pp.
631 Navarro V and Alonso E E (2000) Modelling swelling soils for disposal barriers. Computers and
632 Geotechnics 27:19-43.
633 Ngo V V, Delalande M, Clément A, Michau N and Fritz B (2014) Coupled transport-reaction
634 modeling of the long-term interaction between iron, bentonite and Callovo-Oxfordian claystone
635 in radioactive waste confinement systems. Applied Clay Science 101: 430-443.
636 Nguyen T S, Selvadurai A P S and Armand G (2005) Modelling the FEBEX THM experiment using
637 a state surface approach. International Journal of Rock Mechanical and Minning Science 42
638 (5–6): 639–651.
639 Ochs M, Lothenbach B, Wanner H, Sato H and Mikazu Y (2001) An integrated sorption-diffusion
640 model for the calculation of consistent distribution and diffusion coefficients in compacted
641 bentonite. Journal of Contaminant Hydrology 47: 283–296.
642 Olson S and Karnland O (2011) Mineralogical and chemical characteristics of the bentonite in the
643 A2 test parcel of the LOT field experiments at Äspö HRL, Sweden. Physics and Chemistry of
644 the Earth, Parts A/B/C 36 (17–18): 1545–1553.
645 Ortiz L, Volckaert G and Mallants D (2002). Gas generation and migration in Boom clay, a
646 potential host rock formation for nuclear waste storage. Engineering Geology 64: 287-296.
647 Pollock D W (1986) Simulation of fluid flow and energy transport processes associated with high-
648 level radioactive waste disposal in unsaturated alluvium. Water Resources Research 22 (5):
649 765–775.
650 Samper J, Yang C and Montenegro L (2003) CORE^{2D} version 4: a code for non-isothermal water
651 flow and reactive solute transport. User's Manual. University of A Coruña, Spain.
652 Samper J, Yang C, Montenegro L, Bonilla M, Lu C, Yang Q and Zheng L(2007) Mass and energy
653 balance and flux calculations for radionuclide release and geochemical evolution for SF carbon
654 steel HLW repositories in clay and granite. NF-PRO Project. Deliverable D5.1.13. University
655 of A Coruña, Spain.
656 Samper J, Zheng L, Montenegro L, Fernández A M and Rivas P (2008a) Testing coupled thermo-
657 hydro-chemical models of compacted bentonite after dismantling the FEBEX in situ test.
658 Applied Geochemistry (23/5): 1186–1201.

659 Samper J, Zheng L, Fernández A M and Montenegro L (2008b) Inverse modeling of
660 multicomponent reactive transport through single and dual porosity media. Journal of
661 Contaminant Hydrology 98(3-4): 115-127.
662 Samper J, Lu C and Montenegro L (2008c) Reactive transport model of interactions of corrosion
663 products and bentonite Physics and Chemistry of the Earth33(1): 306-316.
664 Samper, J., Xu, T., Yang, C. (2009). A sequential partly iterative approach for multicomponent
665 reactive transport with CORE^{2D}. Computat. Geosci., 13:301 https://doi.org/10.1007/s10596-
666 008-9119-5.
667 Samper J, Naves A, Montenegro L, Mon A (2016) Reactive transport modelling of the long-term
668 interactions of corrosion products and compacted bentonite in a HLW repository in granite:
669 Uncertainties and relevance for performance assessment. Applied Geochemistry 67: 42-51.
670 Samper J, Mon A and Montenegro L (2018) A revisited thermal, hydrodynamic, chemical and
671 mechanical model of compacted bentonite for the entire duration of the FEBEX in situ test,
672 Applied Clay Science 160: 58–70.
673 Sánchez M, Gens A, Guimarães LJDN and Olivella S (2005) A double structure generalized
674 plasticity model for expansive materials. International Journal for Numerical and Analytical
675 Methods in Geomechanics 29: 751–787.
676 Sánchez M, Gens A and Olivella S (2012a) THM analysis of a large-scale heating test
677 incorporating material fabric changes. International Journal for numerical and analytical
678 methods in Geomechanics 36: 391-421.
679 Sánchez M, Gens A andGuimarães L (2012b) Thermal–hydraulic–mechanical (THM) behavior of
680 a large-scale in situ heating experiment during cooling and dismantling, Canadian
681 Geotechnical Journal, 49(10): 1169-1195.
682 Sánchez M, Arson C, Gens A and Aponte F (2016a) Analysis of unsaturated materials hydration
683 incorporating the effect of thermo-osmotic flow. Geomechanics for Energy and Environment
684 6: 101-115.
685 Sánchez M, Gens A, Villar MV and Olivella S (2016b) Fully coupled Thermo-Hydro-Mechanical
686 Double-Porosity formulation for unsaturated soils. International Journal of Geomechanics 16
687 (6), art. No. 4016015.
688 Savage D, Watson C, Benbow S and Wilson J (2010) Modelling iron-bentonite interactions,
689 Applied Clay Science 47: 91-98.
690 Savage D (2012) Prospects for coupling modelling. STUK-TR 13, Radiation and Nuclear Safety
691 Authority.
692 Sedighi M and Thomas H (2014). Micro porosity evolution in compacted swelling clays – A
693 chemical approach. Applied Clay Science 101: 608–618.
694 Sedighi M, Thomas H R and Vardon P J (2018) Reactive transport of chemicals in compacted
695 bentonite under nonisothermal water infiltration. Journal of Geotechnical and
696 Geoenvironmental Engineering, 144(10), art. no. 04018075.
697 Soler J M (2001) The effect of coupled transport phenomena in the Opalinus clay and implications
698 for radionuclide transport. Journal of Contaminant Hydrology 53: 63–84.

699 Soler, J.M., Samper, J., Yllera, A., Hernández, A., Quejido, A., Fernández, M., Yang, C., Naves,
700 A., Hernán, P., Wersin, P., (2008). The DI-B in-situ diffusion experiment at Mont Terri: results
701 and modelling. Phys. Chem. Earth, 33(1), S196-S207.
702 Tournassat C (2003) Cations-clay interactios: the Fe(II) case. Application to the problematic of
703 the French deep nuclear repository field concept. Ph.D. Dissertation, Grenoble, France.
704 Tournassat C and Appelo C A J (2011) Modelling approaches for anion-exclusion in compacted
705 Na-bentonite. Geochimica et Cosmochimica Acta 75: 3698–3710.
706 Verstricht J, Van Humbeeck H, Li X L and De Cannière P (2007). Final report on the mock-up
707 "OPHELIE, EIG EURIDICE". 197 pp.
708 Villar MV, Martin P, Lloret A and Romero E (2004) Final report on thermo-hydro-mechanical
709 laboratory test. FEBEX II. ENRESA Technical Report: 70-IMA-L-0-97, 2004.
710 Villar M V, Fernández A M, Martín P L, Barcala J M, Gómez-Espina R and Rivas P (2008a) Effect
711 of heating/hydration on compacted bentonite: test in 60 cm long cells. Colección Documentos
712 CIEMAT.
713 Villar M V, Sánchez M and Gens A (2008b) Behaviour of a bentonite barrier in the laboratory:
714 experimental results up to 8 years and numerical simulation. Physics and Chemistry of the
715 Earth 33(1): 476-485.
716 Villar M V, Martín P L, Bárcena I, García-Sinériz J L, Gómes-Espina R and Lloret A (2012) Long-
717 term experimental evidences of saturation of bentonite under repository conditions.
718 *Engineering Geology,* 149-150: 57-69.
719 Villar M V, Iglesias R, Gutiérrez-Alvarez C and Carbonel B (2018) Hydraulic and mechanical
720 properties of compacted bentonite after 18 years in barrier conditions. Applied Clay Science
721 160: 49–57.
722 Villar M V, Iglesias R and García-Siñeriz J L (2019) State of the in situ Febex test (GTS,
723 Switzerland) after 18 years: a heterogeneous bentonite barrier. Environmental Geotechnics,
724 0: 1-13.
725 Wersin P, Birgersson M, Olsson S, Karland O and Snellman M (2007) Impact of corrosion-derived
726 iron on the bentonite buffer within KBS-3H disposal concept- the Olkilouto Site as case study.
727 Posiva Technical Report, pp. 61.
728 Wollery T J (1992) EQ3/3. A software package for geochemical modeling of aqueous system:
729 package overview and installation guide version 7.0. UCRL-MA-110662-PT-I, Lawrence
730 Livermore National Laboratory, Livermore, California.
731 Yang C, Samper J, Montenegro L (2008) A coupled non-isothermal reactive transport model for
732 long-term geochemical evolution of a HLW repository in clay. Environmental Geology 53:
733 1627-1638.
734 Zheng L and Samper J (2004) Formulation of the inverse problem of non-isothermal multiphase
735 flow and reactive transport in porous media. Developments in Water Science 55(2): 1317-
736 1327.

737 Zheng L and Samper J (2005) A dual continuum coupled multiphase flow model with mixed
738 second order water transfer term for structured soils. Jornadas de la Zona no Saturada 2005,
739 VII, 301-306.
740 Zheng L and Samper J (2008) Coupled THMC model of FEBEX mock-up test. Physics and
741 Chemistry of the Earth 33: 486-498.
742 Zheng L, Samper J, Montenegro L and Fernández A M (2010) A coupled THMC model of a
743 heating and hydration laboratory experiment in unsaturated compacted FEBEX bentonite.
744 Journal of Hydrology 386: 80-94..
745 Zheng L, Samper J and Montenegro L (2011) A coupled THC model of the FEBEX in situ test
746 with bentonite swelling and chemical and thermal osmosis. Journal of Contaminant Hydrology
747 126: 45-60.
748 Zheng L and Samper J (2015) Dual-continuum multicomponent reactive transport with nth-order
749 solute transfer terms for structured porous media. Computational Geoscience 19:709–726.
750

751 **Figure captions (images as individual files separate to your MS Word text file).**
752

753 Figure 1. Scheme of a HLW repository in crystalline rock according to the Spanish Reference
754 Concept in the upper-left illustration (Enresa, 2000b). The image of the FEBEX in situ test (upper-
755 right illustration) mimics a disposal cell (http://www.grimsel.com/gts-phase-vi/febex-dp/febex-dp-
756 introduction). The lower-left image shows a sketch of the FEBEX mock-up test (Martín et al.,
757 2006). The lower-right diagram corresponds to the 60 cm-long column tests reported by Villar et
758 al. (2008a).
759

760 Figure 2. Schemes and finite element meshes used in the models of the FEBEX in situ test (Zheng
761 et al., 2011, Samper et al., 2018), the FEBEX mock-up test (Zheng and Samper, 2008), the 60
762 cm-long CG column HHT (Mon, 2017), and the HLW repository in granite (Samper et al., 2016).
763

764 Figure 3. Left axis: Computed (line) (Mon, 2017) and measured (symbols) water intake (Villar et
765 al., 2008a) for the CG7.6 column HHT with and without bentonite swelling. Right axis: Computed
766 (line) (Zheng and Samper, 2008) and measured (symbols) water intake (Martín et al., 2006) for
767 the FEBEX *mock-up* test.
768

Figure 4. Spatial distribution of the measured (symbols) (Villar et al., 2008a) and computed (line) (Mon, 2017) gravimetric water content (top left) and porosity (down left) at the end of the CG0.5, CG0.5b, CG1, CG1b, CG2, CG2b and CG7.6 columns HHT with bentonite swelling and CG0.5 and CG7.6 column HHT without bentonite swelling; spatial distribution of the computed (Zheng and Samper, 2008) porosity and water content for the FEBEX mock-up test after 2 and 20 years (top right); and spatial distribution of the measured (symbols) (Villar et al., 2018; 2019) and computed (lines) (Samper et al., 2018) gravimetric water content and porosity for the FEBEX in situ test after 5 and 18 years (down right).

Figure 5. Top plot: Spatial distribution of the measured (symbols) (Villar et al., 2008a) and the computed (lines) (Mon, 2017) concentrations of dissolved Cl^- at the end of the CG0.5, CG0.5b, CG1, CG1b, CG2, CG2b and CG7.6 columns HHT with and without bentonite swelling for CG0.5 and CG7.6 column HHT. Bottom plot: Radial distribution of the concentrations of the computed concentrations of dissolved Cl^- in the FEBEX in situ test after 0.5, 1, 2, 5, 7.5 and 18 years (Samper et al., 2018) and measured concentration of Cl^- from aqueous extracts (Zheng et al., 2011 and Fernández et al., 2018).

Figure 6. Spatial distribution of the computed cumulative dissolution/precipitation of calcite for the CG column HHT (left axis) and the FEBEX in situ test (right axis). Positive values for precipitation and negative for dissolution.

Figure 7. Spatial distribution of the computed cumulative dissolution/precipitation of gypsum for the CG column HHT (left axis) and the FEBEX in situ test (right axis). Positive values for precipitation and negative for dissolution.

Figure 8. Spatial distribution of the computed cumulative dissolution/precipitation of anhydrite for the CG column HHT (left axis) and the FEBEX in situ test (right axis). Positive values for precipitation and negative for dissolution.

Figure 9. Spatial distribution of the computed pH for the CG column HHT (left axis) and the FEBEX in situ test (right axis).

Figure 10. Time evolution of the temperature at the canister and canister corrosion rate for a 1Ma simulation of a HLW repository in granite (top) and computed cumulative magnetite and siderite precipitation in the bentonite barrier after 10^4 y and 1 Ma (bottom). Notice that the canister/bentonite interface is located at 4.5 dm from the gallery axis (modified from Samper et al., 2016).

Appendix 1. Mathematical formulation

This appendix presents the mathematical formulation of the coupled THMC model. This formulation has been extracted from Zheng et al. (2011).

Water mass balance is given by (Navarro and Alonso, 2000):

$$\frac{D_s m^w}{Dt} + m^w \nabla \cdot \boldsymbol{v}^s + \nabla \cdot \left(\rho^l X_l^w \boldsymbol{q}^l + \rho^g X_g^v \boldsymbol{q}^g + \boldsymbol{j_v}\right) = 0$$

1.

where $\frac{D_s()}{Dt}$ is the material derivative with respect to the solid particles, which move with a velocity vector $\boldsymbol{v}^s$ (m/s), $\nabla \cdot ( )$ is the divergence operator, ρ^l and ρ^g are the bulk densities of the liquid and gaseous phases (kg/m^3), respectively, X_l^w is the mass fraction of water in the liquid phase, X_g^v is the mass fraction of the vapor in the gas phase, $\boldsymbol{q^l}$ is the vector of volumetric liquid flux (m/s) which is given by Eq. 18, $\boldsymbol{q^g}$ is the vector of volumetric gas flux (m/s), which is given by Eq. 19, $\boldsymbol{j_v}$ is the dispersive mass flux of vapor with respect to the mean gas velocity (kg/m^2/s), which is given by Eq. 20, and m^w is the mass of water per unit volume of porous medium (kg/m^3), which is given by:

$$m^w = \emptyset\left[\rho^l X_l^w S_l + \rho^g X_g^v (1 - S_l)\right]$$

2.

where $\emptyset$ is the porosity and S_l is the liquid saturation degree.

The air mass balance equation is given by:

826 $$\frac{D_s m^a}{Dt} + m^a \nabla \cdot \boldsymbol{v^s} + \nabla \cdot \left(\rho^g X_g^a \boldsymbol{q^g} + \rho^l X_l^a \boldsymbol{q^l}\right) = 0$$

827 3.

828 where X_g^a is the mass fraction of air in the gaseous phase, X_l^a is the mass fraction of air in the

829 liquid phase, and m^a is the mass of air per unit volume of porous medium (kg/m^3) which is given

830 by:

831 $$m^a = \emptyset\left[\rho^g X_g^a (1 - S_l) + \rho^l X_l^a S_l\right]$$

832 4.

833 The solid mass balance is given by:

834 $$\frac{D_s \rho^d}{Dt} + \rho^d \nabla \cdot \boldsymbol{v^s} = 0$$

835 5.

836 where ρ^d is the dry density of the medium, which is equal to $\rho^s(1 - \emptyset)$, where ρ^s is the density of

837 the solid particles (kg/m^3). If the coefficient of the thermal expansion of the solid particles (1/ºC),

838 C_T^s, is considered and the mechanical compressibility of the particles C_p^s is disregarded (C_T^s >> C_p^s),

839 then Eq. 5 becomes:

840 $$\frac{D_s \emptyset}{Dt} = (1 - \emptyset)\left[\nabla \cdot \boldsymbol{v_s} - C_T^s \frac{D_s T}{Dt}\right]$$

841 6.

842 where T is the temperature (ºC).

843 Our formulation assumes that all phases are at local thermal equilibrium and therefore they are

844 all at the same temperature. Hence, the energy balance is described in terms of an equation of

845 internal energy, which is defined by the following balance of enthalpy:

846 $$\frac{D_s h}{Dt} + h \nabla \cdot \boldsymbol{v^s} + \nabla \cdot \left(-\Lambda \cdot \nabla T + \boldsymbol{I^e}\right) = 0$$

847 7.

848 where h is the average specific enthalpy of the soil (J/kg), which in turn is given by:

849 $$h = \rho^l X_l^w \emptyset S_l h^w + \rho^l X_l^a \emptyset S_l h^a + \rho^g X_g^v \emptyset (1 - S_l) h^v + \rho^g X_g^a \emptyset (1 - S_l) h^a + \rho^l X_l^a \emptyset S_l h^a + \rho^s (1 - \emptyset) h^s$$

850 8.

where h^w, h^v, h^a and h^s are the specific enthalpies of free water, vapor, air and solid particles respectively, which are assumed to depend linearly on temperature and specific heat (Navarro and Alonso, 2000):

$$h^w = c_w(T - T_o)$$

9.

$$h^v = c_v(T - T_o) + h_o^v$$

10.

$$h^a = c_a(T - T_o)$$

11.

$$h^s = c_s(T - T_o)$$

12.

where c_w, c_v, c_a and c_s are the specific heat at the temperature T_o of the liquid, vapor, air and solid, respectively; and h_o^v is the specific enthalpy of water vapor at temperature T_o.

$\boldsymbol{I^e}$ is the vector of convective energy flux, which is given by:

$$\boldsymbol{I^e} = \rho^l X_l^w h^w \boldsymbol{q^l} + \rho^g X_g^v h^v \boldsymbol{q^v} + \rho^g X_g^a h^a \boldsymbol{q^g}$$

13.

where $\boldsymbol{q^g}$ is the vector of volumetric vapor flux (m/s), which is given by the last terms of Eq. 1, that is, $\boldsymbol{q^v} = \rho^g X_g^v \boldsymbol{q^g} + \boldsymbol{j^v}$ and $\boldsymbol{\Lambda}$ is the bulk thermal conductivity tensor (W/mºC), which for unsaturated bentonite is computed as a volume-weighted average of the conductivities of the components according to:

$$\boldsymbol{\Lambda} = \emptyset S_l \boldsymbol{\Lambda^w} + X_l^a \emptyset S_l \boldsymbol{\Lambda^a} + \emptyset(1 - S_l)(\boldsymbol{\Lambda^v} + \boldsymbol{\Lambda^a}) + (1 - \emptyset)\boldsymbol{\Lambda^s}$$

14.

where $\boldsymbol{\Lambda^w}$, $\boldsymbol{\Lambda^v}$, $\boldsymbol{\Lambda^a}$ and $\boldsymbol{\Lambda^s}$ are the thermal conductivities of water, vapor, air and solid, respectively. This equation is inspired in the formulation of De Vries's (1963), which according to Tang et al. (2008) provides the best fit to measured thermal conductivity data for several bentonites such as FEBEX bentonite. The formulation in Eq. 14, however, may not be the appropriate for courser porous materials. According to Soler (2001), the Dufour effect is negligible compared to thermal conduction and, therefore, can be disregarded.

Solute transport processes include advection, molecular diffusion, and mechanical dispersion. Each of them produces a solute flux per unit surface and unit time. There are as many transport equations as primary chemical species in the system. The mass balance equation for the j-th primary species is given by (Zheng and Samper, 2008):

$$m_l^w \frac{\partial C_j}{\partial t} + \frac{\partial \left(m_l^w P_j\right)}{\partial t} + \frac{\partial \left(m_l^w W_j\right)}{\partial t} + \frac{\partial \left(m_l^w Y_j\right)}{\partial t} = L^*\left(C_j\right) + r_i\left(C_j^0 - C_j\right) \quad j = 1,2,\dots,N_c$$

15.

where C_j is the total dissolved concentration of the of j-th species (mol/L), m_l^w is the mass of liquid water per unit volume of medium (kg/m^3), which is equal to $\rho^l X_l^w \theta$, where $\theta = S_l \emptyset$ is the volumetric watercontent (m^3/m^3), P_j, Y_j and W_j are the total precipitated, sorbed and exchanged concentrations (mol/L), respectively, of the j-th primary species, r_i is the sink term (kg/m^2/s), C_j^0 is the dissolved concentration of j-th species (mol/L) in the sink term r_i, N_c is the number of primary species. $L^*(\,)$ is the following transport operator:

$$L^*(\,) = \nabla \cdot [m_l^w \boldsymbol{D^j} \cdot \nabla(\,)] - m_l^w \boldsymbol{q^l} \cdot \nabla(\,) + (r_e - r_c)(\,)$$

16.

where $\boldsymbol{D^j}$ is the dispersion coefficient (m^2/s), and r_c and r_e are the condensation and evaporation rates (kg/m^2/s), respectively. The dispersion coefficient $\boldsymbol{D^j}$ includes the hydrodynamic or mechanical dispersion, D_h , and the porewater molecular diffusion, D_m, which is related with the molecular diffusion in pure water, D_o, through:

$$D_m = S_l \emptyset D_o \tau$$

17.

where τ is the medium tortuosity.

Thermal and chemical osmosis contribute to the volumetric liquid flux, $\boldsymbol{q^l}$, according to (Keijzeret al., 1999; Keijzer and Loch, 2001; Soler, 2001):

$$\boldsymbol{q^l} = -\frac{\boldsymbol{K^{il}} k^{rl}}{\mu^l}(\nabla p^l + \rho^l g \nabla z) - k_T \nabla T + \sigma \frac{\boldsymbol{K^{il}} k^{rl}}{\mu^l} \nabla \pi_h$$

18.

where p^l is the liquid pressure (Pa), $\boldsymbol{K^{il}}$ is the intrinsic permeability tensor of the liquid (m^2), k^{rl} is the relative permeability of the liquid, μ^l is the viscosity of the liquid (kg/m/s), z is the elevation,

k_T is the thermal-osmotic permeability (m²/K/s), π_h is the osmotic pressure (Pa), and σ is a dimensionless reflection coefficient for chemical osmosis . The volumetric gas flux, $\boldsymbol{q^g}$, is given by:

$$\boldsymbol{q^g} = -\frac{\boldsymbol{K^{ig}} k^{rg}}{\mu^g}(\nabla p^g + \rho^g g \nabla z)$$

19.

where $\boldsymbol{K^{ig}}$ is the intrinsic permeability tensor of the gas (m²), k^{rg} is the relative permeability of gas, μ^g and is the viscosity of the gas phase (kg/m/s).

The dispersive mass flux of vapor , $\boldsymbol{j^v}$, is calculated by the Fick's law:

$$\boldsymbol{j^v} = -\rho^g \boldsymbol{D^v} \nabla X_g^v$$

20.

where $\boldsymbol{D^v}$ is the hydrodynamic dispersion tensor for vapor (m²/s) which includes the effects of mechanical dispersion (D_{disp}) and molecular diffusion (D_e^v). The effective molecular diffusion coefficient for the vapor was calculated from Pollock (1986):

$$D_e^v = \frac{5.9 \cdot 10^{-6} \tau^v (T + 273.15)^{2.3}}{p^g}$$

21.

where τ^v is the vapor tortuosity factor (dimensionless).

The following incremental formulation of the equilibrium equation of Navarro and Alonso (2000) is used:

$$\nabla \cdot (\Delta \boldsymbol{\sigma}' + \Delta P^g \boldsymbol{\delta}) + \Delta \rho g \boldsymbol{k} = 0$$

22.

where $\Delta\rho$ is the increment of the average soil density, g is the gravitational acceleration (m/s²), $\boldsymbol{k}$ is the unit vector in the gravity direction, $\boldsymbol{\delta}$ is the vector expression of Kronecker's delta, ΔP^g is the increment in gas pressure (Pa) which for saturated conditions should be replaced by the increment in the liquid pressure (Pa), ΔP^l, and $\Delta\boldsymbol{\sigma}'$ is the vector of increments of effective stress (Pa), which is related to the vector of increments of total stress $\Delta\boldsymbol{\sigma}$ (Pa) in unsaturated conditions through:

$$\Delta \boldsymbol{\sigma}' = \Delta \boldsymbol{\sigma} - \Delta P^g \boldsymbol{\delta}$$

23.

while for saturated conditions the previous equation is replaced by $\Delta\boldsymbol{\sigma}' = \Delta\boldsymbol{\sigma} - \Delta P^l\boldsymbol{\delta}$ (Fredlund and Rahardjo, 1993).

The general constitutive law for the thermomechanical model is defined with the following mechanical law:

$$d\boldsymbol{\varepsilon} = \boldsymbol{C}d\boldsymbol{\sigma}' + \boldsymbol{\beta}d\Psi + \boldsymbol{\alpha}dT \quad (24)$$

where $\boldsymbol{\varepsilon}$ is the strain vector, $\boldsymbol{C}$ is the elastic matrix (1/Pa), $\boldsymbol{\beta}$ is a vector of coefficients (1/Pa), which account for the deformation caused by changes in suction Ψ, $\Psi = (p^l - p^g)$, and $\boldsymbol{\alpha}$ is a vector of thermal expansion coefficients (1/ºC). The standard sign convention used in Soil Mechanics is adopted here according to which compressions are positive. To overcome the difficulties of the different mechanical models, some researchers have resorted to simpler models such as the state-surface approach to simulate bentonite swelling. Nguyen et al. (2005) used successfully the state-surface approach to interpret a swelling pressure test and simulate the FEBEX in situ test. The volumetric deformation caused by bentonite swelling is described by a state surface for the void ratio with the following state-surface expression of Lloret and Alonso (1995):

$$e = A + Bln\sigma' + Cln(\Psi + p^a) + Dln\sigma' \ln(\Psi + p^a) \quad (25)$$

where e is the void ratio, which is equal to the volume of voids divided by the volume of the solids; p^a is the atmospheric pressure in Pa, σ' is the mean effective stress in Pa; Ψ is suction in Pa, and A, B, C and D are empirical constants. The state surface is used to quantify the volume change during the drying or wetting phase with a simple stress path, by taking into account the coupled hydro-mechanical behavior.

The chemical model for compacted bentonite accounts for the following reactions: aqueous complexation, acid/base, redox, cation exchange, surface complexation and mineral dissolution/precipitation. The chemical system is defined in terms of the concentrations of the primary species. The concentrations of the secondary species are computed from the concentrations of the primary species through appropriate mass action laws (Samper et al., 2009). The concentrations of the precipitated, exchanged and adsorbed species are computed using similar equations. A detailed description of the calculations of the chemical reactions can be found in Samper et al. (2009) and Zheng et al. (2011). The Gaines-Thomas convention is used for cation

exchange. Surface complexation is modelled using three types of protonation/deprotonation sites, S^{S}-OH, S^{W1}-OH and S^{W2}-OH, as proposed by Bradbury and Baeyens (1997).

The equilibrium constants for aqueous complexes and minerals depend on temperature under non-isothermal conditions. They are calculated with the following expression, which is valid for temperatures between 0 and 300 ºC:

$$logK(T) = \frac{b_1}{T^2} + \frac{b_2}{T} + b_3 lnT + b_4 + b_5 T \quad 26.$$

where b_1 to b_5 are coefficients, which are derived by fitting Equation 26 to measured $logK$ values at 0, 25, 60, 100 and 300ºC (Wolery, 1992).The thermodynamic database of EQ3/6 (Wolery, 1992) is used for aqueous complexes and minerals.

977 **Appendix 2. Tables of model parameters**

978

979 Table 2. Chemical reactions and equilibrium constants for aqueous complexes and minerals
980 (Wolery, 1992), protolysis constants for surface complexation reactions (Bradbury and Baeyens,
981 1997) and selectivity coefficients for cation exchange (ENRESA, 2006b) at 25ºC considered in
982 the HHT.

Aqueous complexes	Log K (25ºC)
$CaCO_3(aq) + H^+ \Leftrightarrow Ca^{2+} + HCO_3^-$	7.0017
$CaHCO_3^+ \Leftrightarrow Ca^{2+} + HCO_3^-$	-1.0467
$CaSO_4(aq) \Leftrightarrow Ca^{2+} + SO_4^{2-}$	-2.1111
$CaCl^+ \Leftrightarrow Ca^{2+} + Cl^-$	0.6956
$CO_2(aq) + H_2O \Leftrightarrow H^+ + HCO_3^-$	-6.3447
$CO_3^{2-} + H^+ \Leftrightarrow HCO_3^-$	10.3288
$KSO_4^- \Leftrightarrow K^+ + SO_4^{2-}$	-0.8796
$MgCO_3(aq) \Leftrightarrow Mg^{2+} + CO_3^{2-}$	-2.9789
$MgHCO_3^+ \Leftrightarrow Mg^{2+} + HCO_3^-$	-1.0357
$MgSO_4(aq) \Leftrightarrow Mg^{2+} + SO_4^{2-}$	-2.4117
$MgCl^+ \Leftrightarrow Mg^{2+} + Cl^-$	0.1349
$NaHCO_3(aq) \Leftrightarrow Na^+ + HCO_3^-$	-0.1541
$NaSO_4^- \Leftrightarrow Na^+ + SO_4^{2-}$	-0.8200
$NaCl(aq) \Leftrightarrow Na^+ + Cl^-$	0.7770
$H_3SiO_4^- + H^+ \Leftrightarrow SiO_2(aq) + 2H_2O$	9.8120
$OH^- + H^+ \Leftrightarrow H_2O$	13.9951
Minerals dissolution/precipitation	**Log K (25ºC)**
$Calcite + H^+ \Leftrightarrow Ca^{2+} + HCO_3^-$	1.8487
$Anhydrite \Leftrightarrow Ca^{2+} + SO_4^{2-}$	-4.3064
$Gypsum \Leftrightarrow Ca^{2+} + SO_4^{2-} + 2H_2O$	-4.4823
$Chalcedony \Leftrightarrow SiO_2(aq)$	-3.7281
Surface complexation	**Log K_{int}**
$\equiv S^SOH_2^+ \Leftrightarrow \equiv S^SOH + H^+$	-4.5
$\equiv S^SO^- + H^+ \Leftrightarrow S^SOH$	7.9
$\equiv S^{W1} OH_2^+ \Leftrightarrow \equiv S^{W1}OH + H^+$	-4.5
$\equiv S^{W1} O^- + H^+ \Leftrightarrow \equiv S^{W1}OH$	7.9
$\equiv S^{W2} OH_2^+ \Leftrightarrow \equiv S^{W2}OH + H^+$	-6.0
$\equiv S^{W2} O^- + H^+ \Leftrightarrow \equiv S^{W2}OH$	-10.5
Ion exchange	**$K_{Na\text{-}cation}$**
$Na^+ + X\text{-}K \Leftrightarrow K^+ + X\text{-}Na$	0.138
$Na^+ + 0.5\ X_2\text{-}Ca \Leftrightarrow 0.5\ Ca^{2+} + X\text{-}Na$	0.292
$Na^+ + 0.5\ X_2\text{-}Mg \Leftrightarrow 0.5\ Mg^{2+} + X\text{-}Na$	0.281

983

984

985

986 Table 3. Hydrodynamic parameters of the bentonite used in the numerical models of the HHT

987 (ENRESA, 2006a; Zheng et al., 2010; Mon, 2017; Zheng and Samper, 2008; Zheng et al., 2011).

Intrinsic permeability of the liquid, k^{il} (m²) as a function of porosity	$k^{il} = k_0 \frac{\emptyset^3}{(1-\emptyset)^2} \frac{(1-\emptyset_0)^2}{\emptyset_0^3}$ with $\emptyset_o$ = 0.40 k_o= 2.75·10^{-21} (CG column HHT), 3.75·10^{-21} (in situ test) and 3.51·10^{-21} (mock-up test)
Liquid relative permeability k^{rl} as a function of liquid saturation S_l	$k_{rl} = S_l^3$
Retention curve: liquid saturation S_l as a function of suction Ψ (Pa)	$S_l = \frac{(1 - 9.1 \cdot 10^{-7}\Psi)^{1.1}}{[(1 + 5 \cdot 10^{-5}\Psi)^{1.22}]^{0.18}}$
Liquid viscosity (kg/m·s) as a function of temperature T (ºC)	$0.6612 \cdot (T - 44)^{-1.562}$
Liquid density (kg/m³) as a function of liquid pressure p^l and temperature (ºC)	$998.2 \cdot e^{[5 \cdot 10^{-7} \cdot (p^l - 100) - 2.1 \cdot 10^{-4} \cdot (T - 22)]}$
Reference temperature, T_{ref} (ºC)	22
Gas intrinsic permeability (m²)	5·10^{-10}
Gas relative permeability k^{rg}	$k_{rl} = (1 - S_l)^3$
Vapor tortuosity factor	0.4 (CG column HHT), 0.2 (in situ test) and 0.09 (mock-up test)
Gas viscosity (kg/m·s)	1.76·10^{-5}
Solid density (kg/m³)	$2750 \cdot e^{[-2 \cdot 10^{-5} \cdot (T - T_{ref})]}$
Thermo-osmotic permeability (m²/K/s)	4.2·10^{-13}

988

989 Table 4. Thermal parameters of the numerical models of the HHT (ENRESA, 2006a; Zheng et al.,

990 2010; Mon, 2017; Zheng and Samper, 2008; Zheng et al., 2011).

Specific heat of the liquid (J/kg·ºC)	4202
Specific heat of the air (J/kg·ºC)	1000
Specific heat of the vapor (J/kg·ºC)	1620
Specific heat of the solid (J/kg·ºC)	835.5
Thermal conductivity of the liquid (W/m·ºC)	0.6
Thermal conductivity of the air (W/m·ºC)	2.6·10^{-2}
Thermal conductivity of the vapor (W/m·ºC)	4.2·10^{-2}
Thermal conductivity of the solid (W/m·ºC)	1.23
Vaporization enthalpy (J/kg)	2.45·10^{6}

991

992

Table 5. Mechanical parameters of the numerical models of the HHT (ENRESA, 2006a; Zheng et al., 2010; Mon, 2017; Zheng and Samper, 2008; Zheng et al., 2011).

Water mechanical compressibility (Pa^{-1})	$5 \cdot 10^{-7}$
Water thermal expansion (K^{-1})	$2.1 \cdot 10^{-4}$
Solid thermal expansion (K^{-1})	$2 \cdot 10^{-5}$
State surface constants (Nguyen et al., 2005)	A = 0.76; B = -0.052446; C = -0.0406413; D = 0.00479977

Table 6. Hydrodynamic and transport parameters of the numerical models of the HHT (ENRESA, 2006a; Zheng et al., 2010; Mon, 2017; Zheng and Samper, 2008; Zheng et al., 2011).

Molecular diffusion in water $D_0(T)$ in m^2/s as a function of T and the molecular diffusion at the reference temperature T_{ref} (ºC), $D_0(T_{ref})$, with T_{ref} = 22ºC	$D_o(T) = D_o(T_{ref})\frac{T}{T_0}\frac{\mu_0^l}{\mu^l}$ $D_o(T_{ref}) = 2 \cdot 10^{-10}$ (CG column HHT and mock-up test). $D_o(T_{ref}) = 2 \cdot 10^{-11}$ (in situ test) Cl^-, $D_o(T_{ref}) = 9 \cdot 10^{-11}$ (CG column HHT and mock-up test) and $D_o(T_{ref}) = 3 \cdot 10^{-12}$ (in situ test) SO_4^{2-} $D_o(T_{ref}) = 3.6 \cdot 10^{-13}$ (in situ test)
Longitudinal dispersivity (m)	0.01
Solute tortuosity τ as a function of volumetric water content θ and porosity ∅	$\tau = \frac{\theta^{7/3}}{\emptyset^2}$

Table 7. Chemical compositions (mol/L) of the initial bentonite porewater and the granitic hydration waters used in the numerical models of the HHT.

	Initial bentonite porewater (Fernández et al., 2001)	Granitic hydration water CG column HHT (Villar et al., 2008a)	Granitic hydration water mock-up test (ENRESA, 2006b)	Grimsel granitic hydration water for in situ test (Samper et al., 2008a)
Na^+	$1.3 \cdot 10^{-1}$	$4.8 \cdot 10^{-4}$	$6.08 \cdot 10^{-4}$	$3.8 \cdot 10^{-4}$
Ca^{2+}	$2.2 \cdot 10^{-2}$	$1.1 \cdot 10^{-3}$	$9.5 \cdot 10^{-4}$	$1.8 \cdot 10^{-4}$
Mg^{2+}	$2.3 \cdot 10^{-2}$	$3.9 \cdot 10^{-4}$	$3.9 \cdot 10^{-4}$	$1.3 \cdot 10^{-6}$
K^+	$1.7 \cdot 10^{-3}$	$2.6 \cdot 10^{-5}$	$3.32 \cdot 10^{-4}$	$7.8 \cdot 10^{-6}$
SO_4^-	$3.2 \cdot 10^{-2}$	$1.5 \cdot 10^{-4}$	$1.56 \cdot 10^{-4}$	$7.9 \cdot 10^{-5}$
Cl^-	$1.6 \cdot 10^{-1}$	$3.7 \cdot 10^{-4}$	$4.23 \cdot 10^{-4}$	$1.3 \cdot 10^{-5}$
$SiO_2(aq)$	$1.0 \cdot 10^{-4}$	$1.9 \cdot 10^{-4}$	$3.62 \cdot 10^{-4}$	$1.4 \cdot 10^{-4}$
HCO_3^-	$5.8 \cdot 10^{-4}$	$2.3 \cdot 10^{-3}$	$2.53 \cdot 10^{-3}$	$3.9 \cdot 10^{-4}$
pH	7.72	8.3	8.1	8.35

1005 Table 8. Initial mineral volume fractions (ENRESA, 2006b), initial concentrations of exchanged
1006 cations (Fernández et al., 2004) and total concentrations of surface complexation sites (Bradbury
1007 and Baeyens, 1997; Bradbury and Baeyens, 2003) used in the numerical models of the HHT.

Initial volume fractions of minerals (vol %)	
Calcite	1.0
Gypsum	0.08
Anhydrite	0.0
Chalcedony	0.45
Smectite	53.48
Initial concentrations of surface complexes (mol/L)	
S^SOH	0.015
$S^{w1}OH$	0.307
$S^{w2}OH$	0.307
Initial concentrations of exchanged cations (meq/100g)	
Ca^{2+}	34.62
Mg^{2+}	34.01
Na^{+}	31.18
K^{+}	1.94

1008
1009
1010 Table 9. Equilibrium constants of minerals (Wolery, 1192; Fernández et al., 2009; Savage et al.,
1011 2010a; Wilkin and Barnes, 1998), protolysis constants of surface complexation reactions for the
1012 triple-site model (Bradbury and Baeyens, 2005), and selectivity constants for cation exchange
1013 reactions (Samper et al., 2008; Tournassat, 2003) at 25ºC used in the model of the long-term
1014 evolution of the EBS.

Minerals dissolution/precipitation	Log K (25ºC)
Carbon steel (canister) + $2H^+ + 0.5O_2(aq) \Leftrightarrow Fe^{2+} + H_2O$	59.033
Calcite + $H^+ \Leftrightarrow Ca^{2+} + HCO_3^-$	1.8487
Gypsum $\Leftrightarrow Ca^{2+} + SO_4^{2-} + 2H_2O$	-4.4823
Quartz $\Leftrightarrow SiO_2(aq)$	-3.9993
Magnetite + $6H^+ \Leftrightarrow 3Fe^{2+} + 0.5O_2(aq) + 3H_2O$	-6.5076
Siderite + $H^+ \Leftrightarrow Fe^{2+} + HCO_3^-$	-0.1920
Goethite + $2H^+ \Leftrightarrow Fe^{2+} + 1.5H_2O + 0.25O_2(aq)$	-7.9555
Surface complexation	**Log K_{int}**
$\equiv S^SOH_2^+ \Leftrightarrow \equiv S^SOH + H^+$	-4.5
$\equiv S^SO^- + H^+ \Leftrightarrow \equiv S^SOH$	7.9
$\equiv S^SOFe^+ + H^+ \Leftrightarrow \equiv S^SOH + Fe^{2+}$	0.6
$\equiv S^SOFeOH + 2H^+ \Leftrightarrow \equiv S^SOH + Fe^{2+} + H_2O$	10.0
$\equiv S^SOFe(OH)_2^- + 2H^+ \Leftrightarrow \equiv S^SOH + Fe^{2+} + 2H_2O$	20.0
$\equiv S^{W1}OH_2^+ \Leftrightarrow \equiv S^{W1}OH + H^+$	-4.5
$\equiv S^{W1}O^- + H^+ \Leftrightarrow \equiv S^{W1}OH$	7.9
$\equiv S^{W1}OFe^+ + H^+ \Leftrightarrow \equiv S^{W1}OH + Fe^{2+}$	3.3
$\equiv S^{W2}OH_2^+ \Leftrightarrow \equiv S^{W2}OH + H^+$	-6.0
$\equiv S^{W2}O^- + H^+ \Leftrightarrow \equiv S^{W2}OH$	-10.5
Ion exchange	**$K_{Na\text{-}cation}$**
$Na^+ + X\text{-}K \Leftrightarrow K^+ + X\text{-}Na$	0.138
$Na^+ + 0.5\ X_2\text{-}Ca \Leftrightarrow 0.5\ Ca^{2+} + X\text{-}Na$	0.292
$Na^+ + 0.5\ X_2\text{-}Mg \Leftrightarrow 0.5\ Mg^{2+} + X\text{-}Na$	0.281
$Na^+ + 0.5\ X_2\text{-}Fe \Leftrightarrow 0.5\ Fe^{2+} + X\text{-}Na$	0.5

1015 Table 10. Chemical composition of the granite boundary water and the initial bentonite porewater,

1016 used in the model of the long-term evolution of the EBS (Samper et al., 2016).

	Bentonite porewater	Boundary granite water
ph	6.46	7.825
Eh (V)	-0.078	-0.188
Ca^{2+} (mol/L)	$3.32 \cdot 10^{-2}$	$1.522 \cdot 10^{-4}$
Mg^{2+} (mol/L)	$3.67 \cdot 10^{-2}$	$1.604 \cdot 10^{-4}$
Na^{+} (mol/L)	$1.88 \cdot 10^{-1}$	$4.350 \cdot 10^{-3}$
K^{+} (mol/L)	$1.55 \cdot 10^{-3}$	$5.371 \cdot 10^{-5}$
Fe^{2+} (mol/L)	$1.43 \cdot 10^{-4}$	$1.791 \cdot 10^{-8}$
Cl^{-}	$2.75 \cdot 10^{-1}$	$3.949 \cdot 10^{-4}$
HCO_3^{-}	$7.59 \cdot 10^{-3}$	$5.049 \cdot 10^{-3}$
SO_4^{2-}	$2.05 \cdot 10^{-2}$	$1.561 \cdot 10^{-5}$
$SiO_2(aq)$	$9.67 \cdot 10^{-5}$	$3.761 \cdot 10^{-4}$

1017

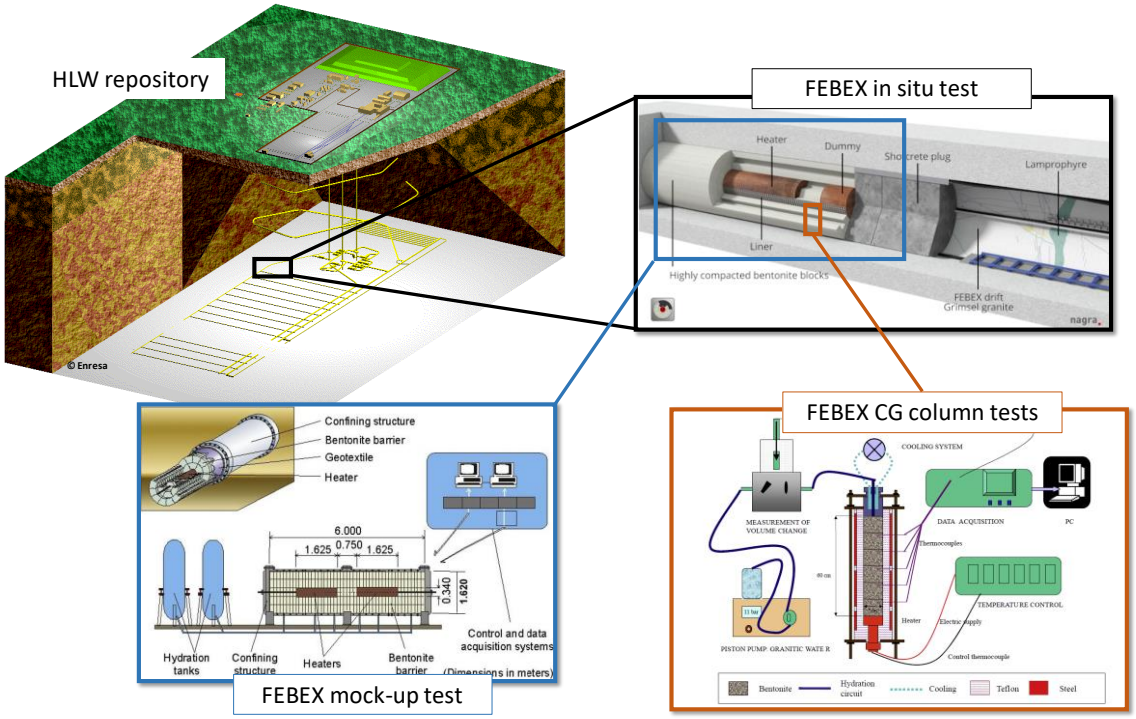


Figure 1

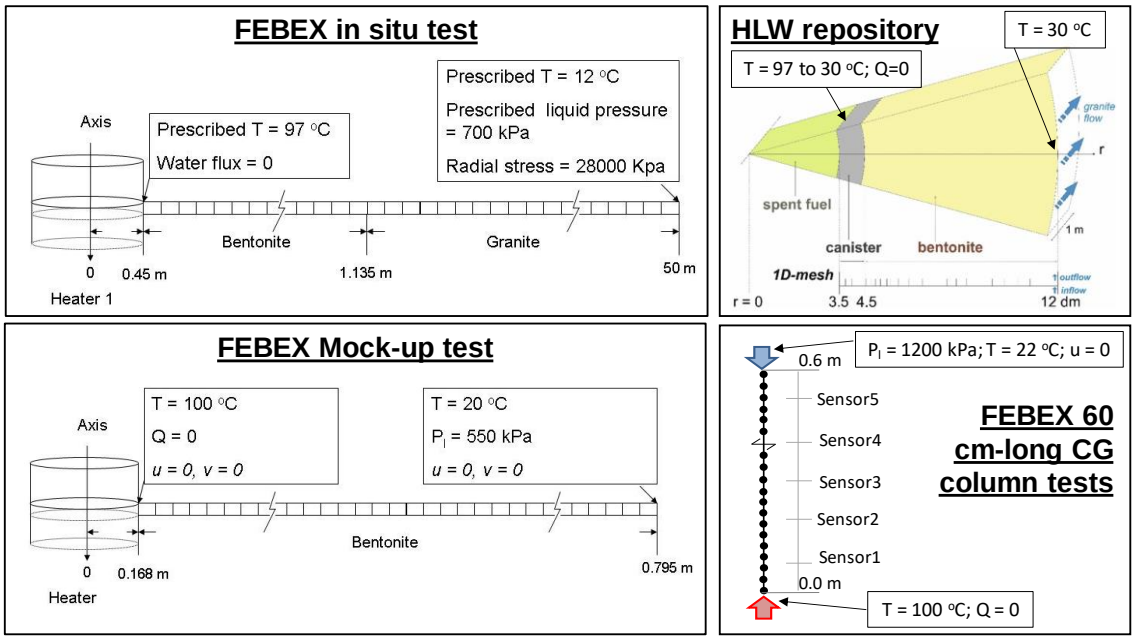


Figure 2

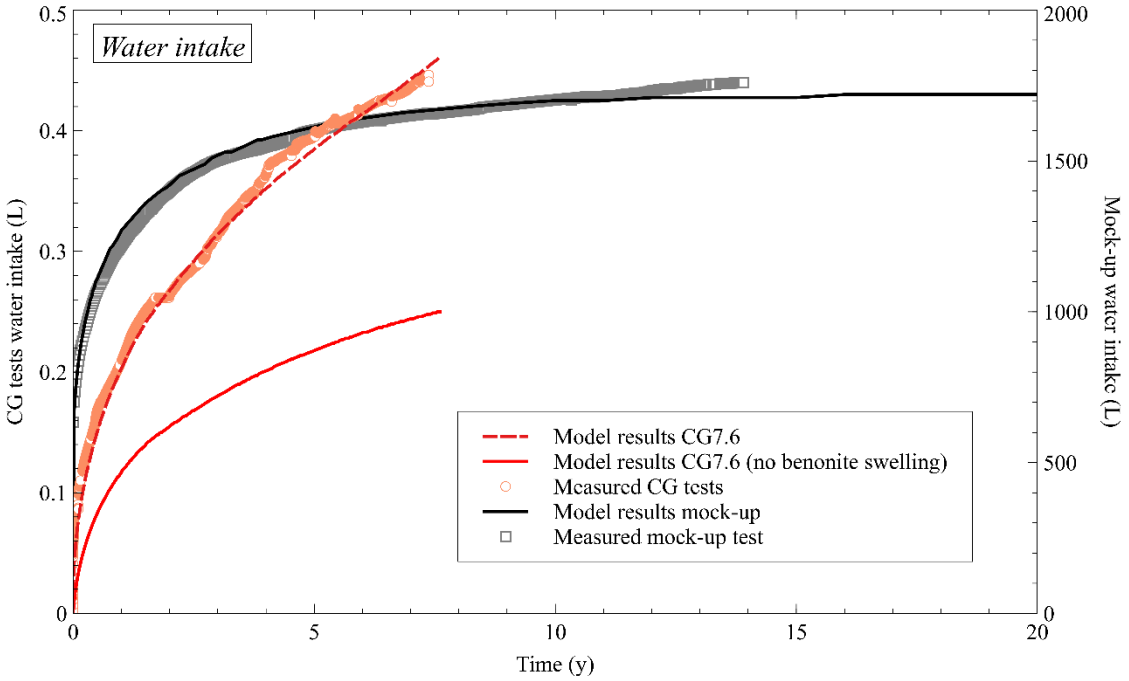


Figure 3

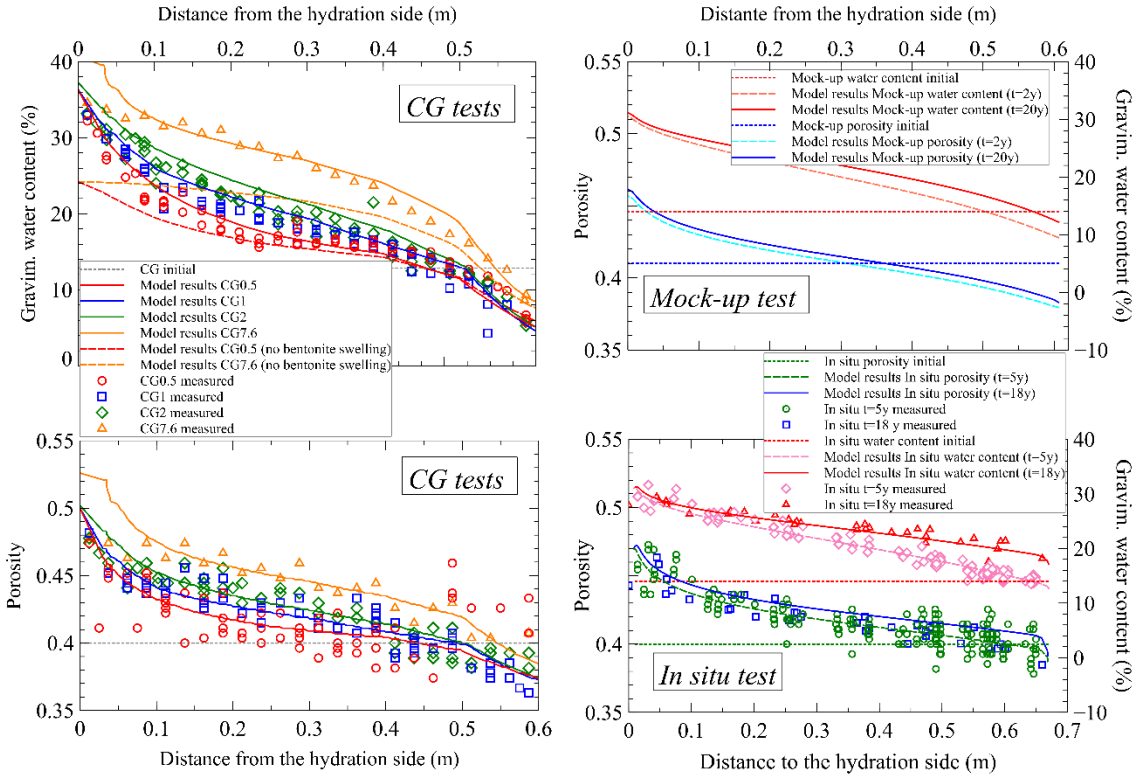
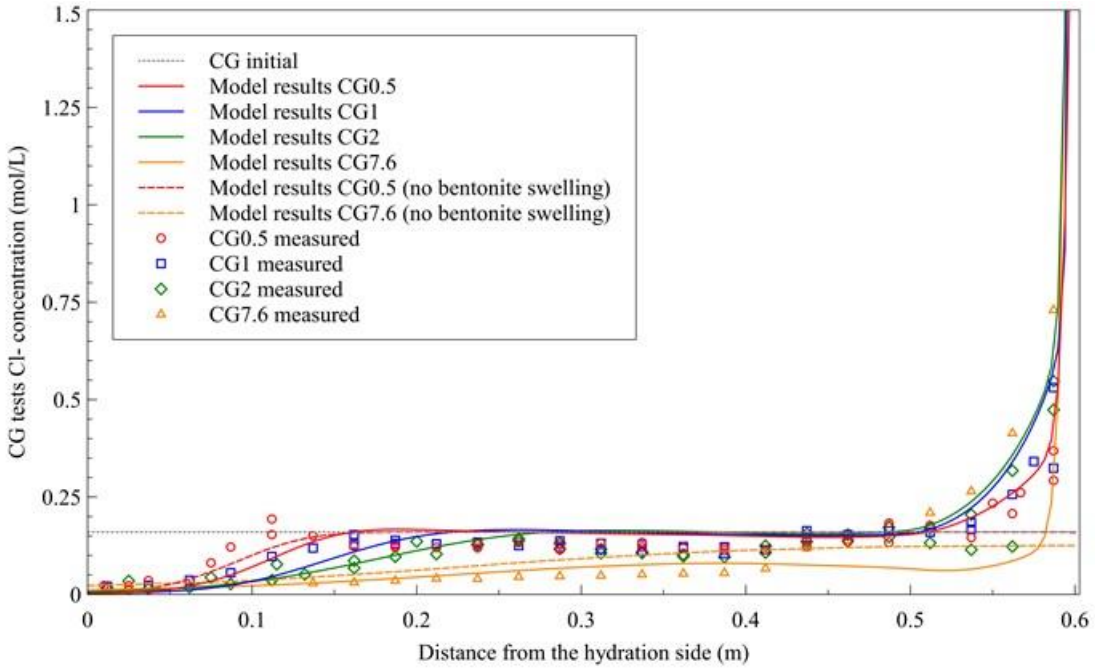


Figure 4


CG initial
Model results CG0.5
Model results CG1
Model results CG2
Model results CG7.6
Model results CG0.5 (no bentonite swelling)
Model results CG7.6 (no bentonite swelling)
CG0.5 measured
CG1 measured
CG2 measured
CG7.6 measured
CG tests Cl- concentration (mol/L)
Distance from the hydration side (m)

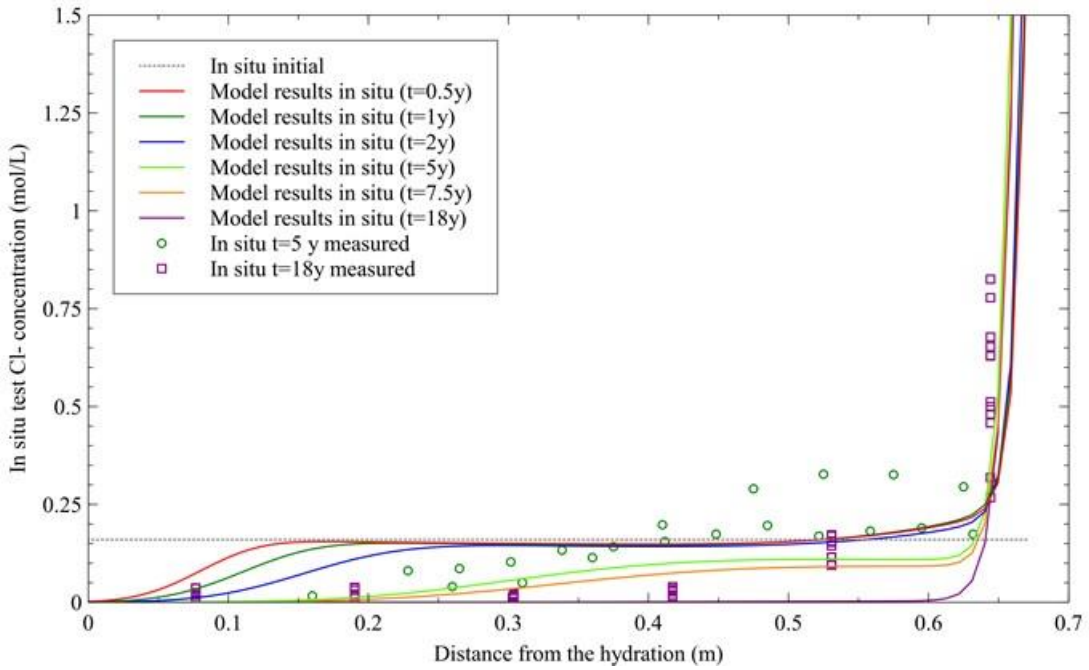

In situ initial
Model results in situ (t=0.5y)
Model results in situ (t=1y)
Model results in situ (t=2y)
Model results in situ (t=5y)
Model results in situ (t=7.5y)
Model results in situ (t=18y)
In situ t=5 y measured
In situ t=18y measured
In situ test Cl- concentration (mol/L)
Distance from the hydration (m)

Figure 5

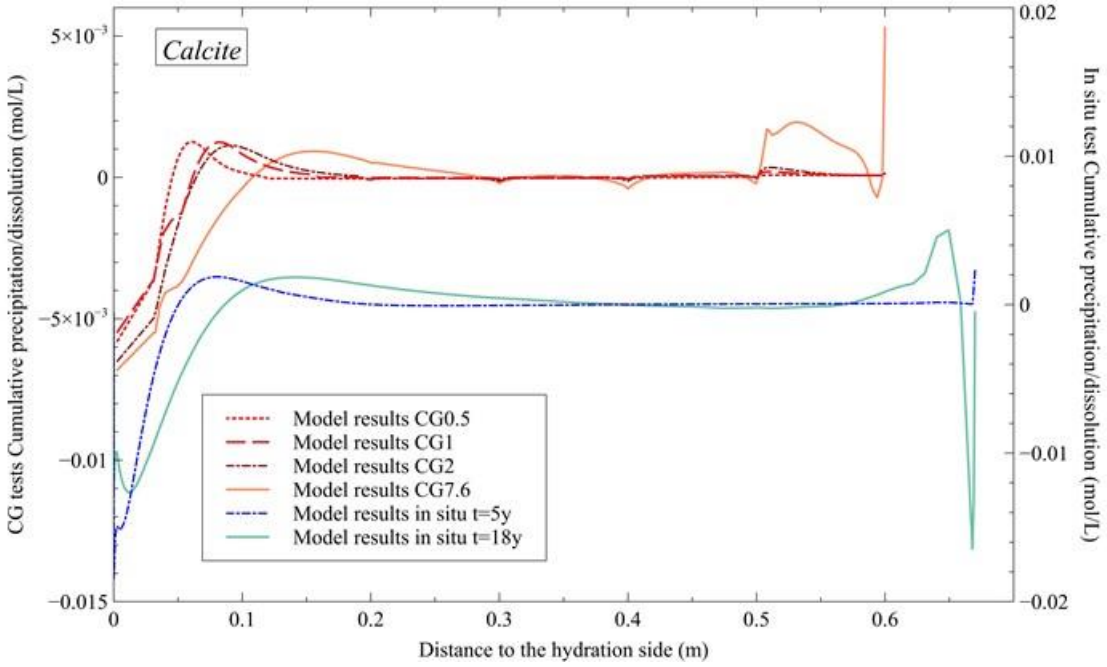


Figure 6

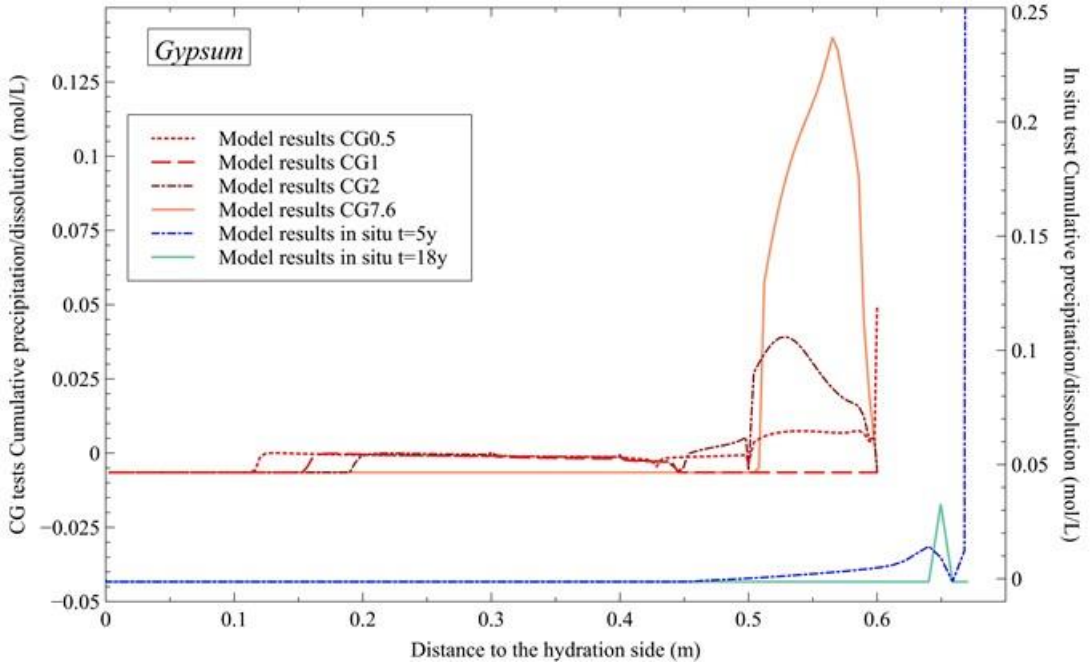


Figure 7

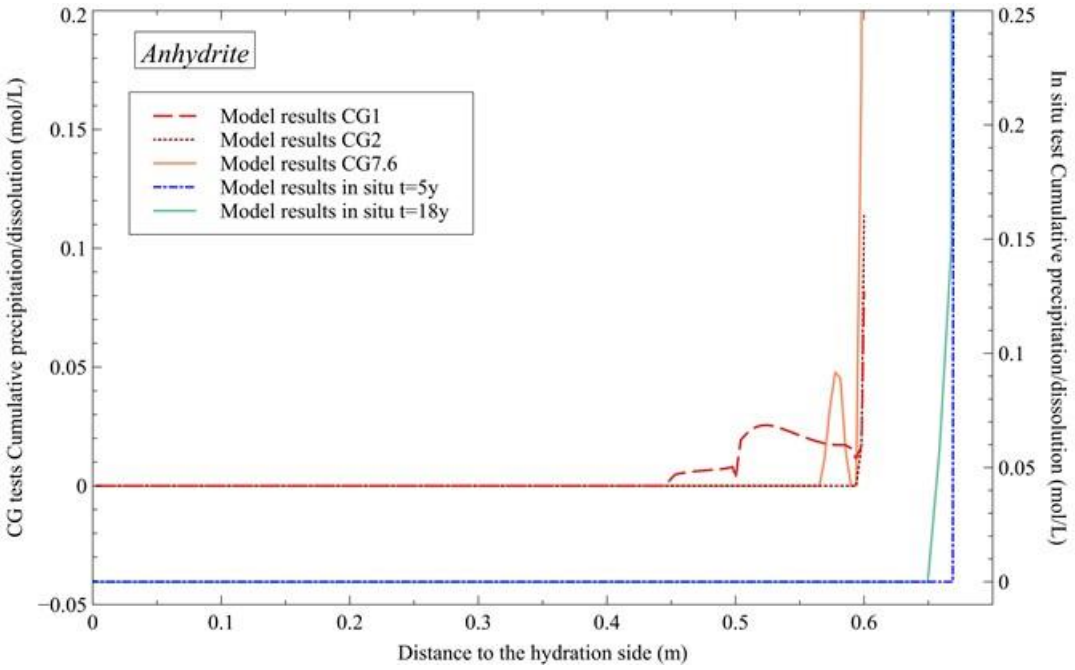


Figure 8

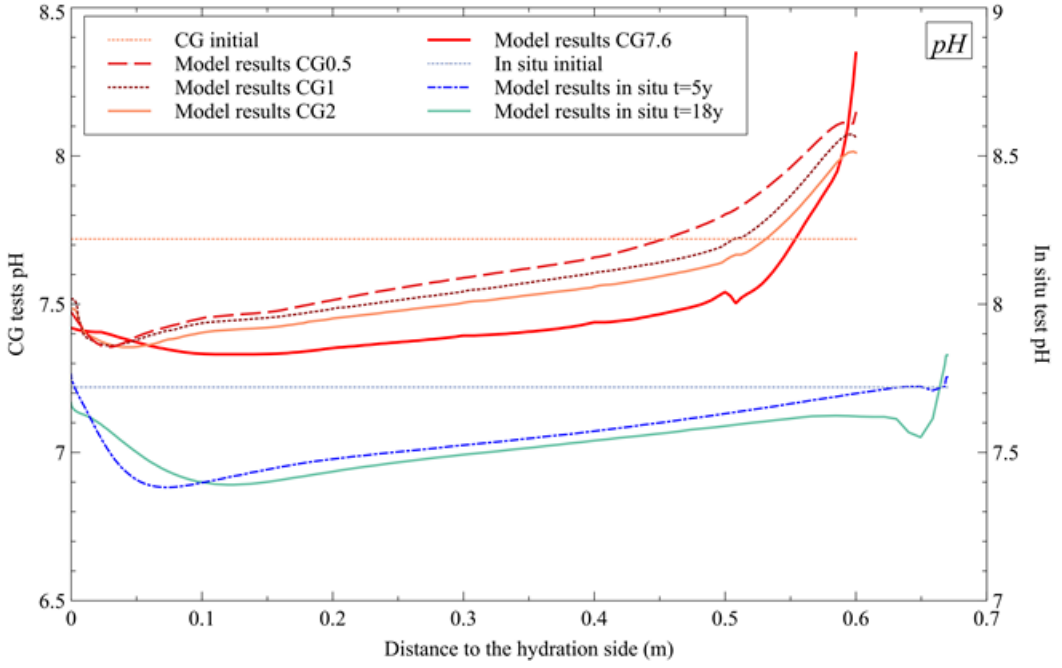


Figure 9

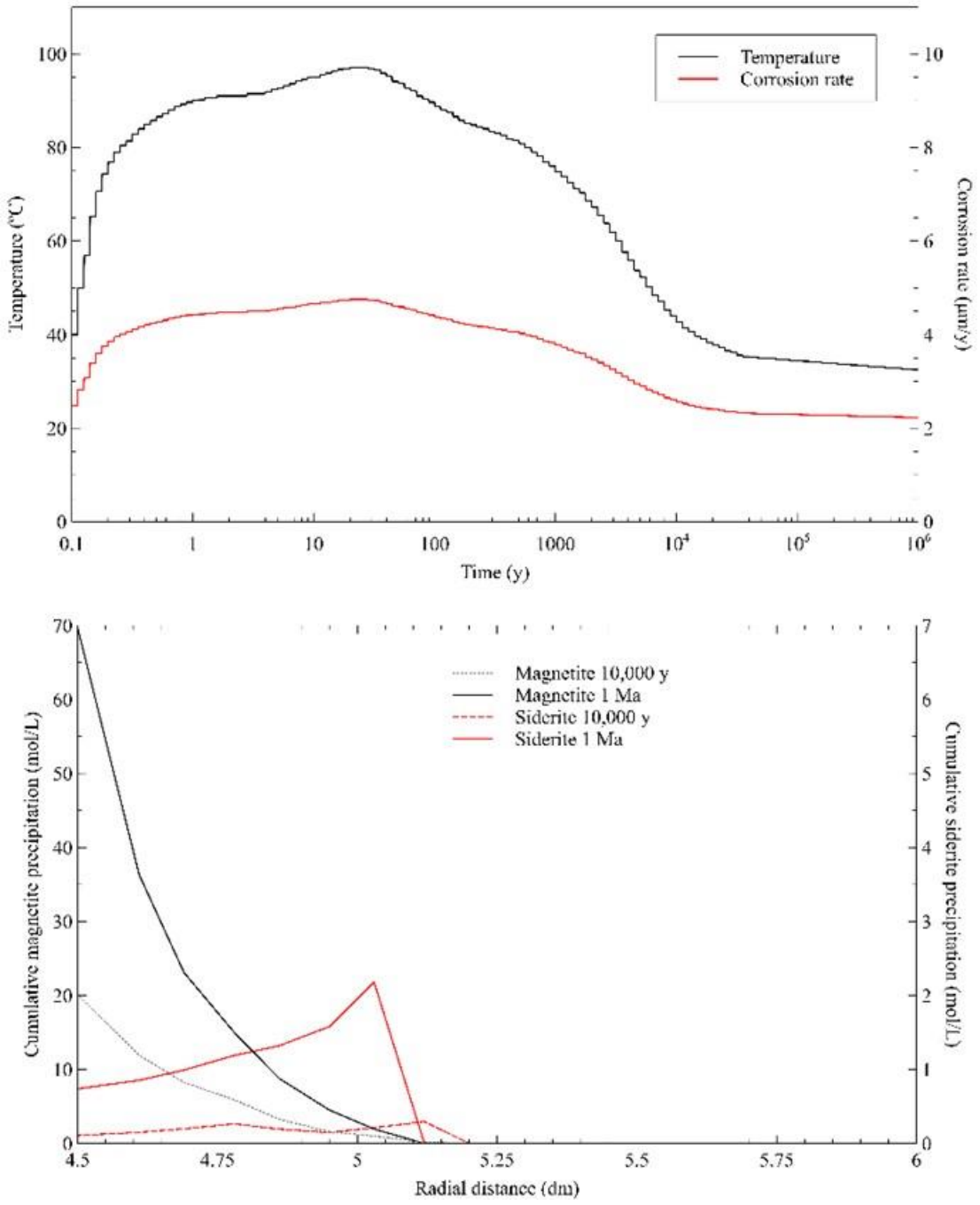

Temperature
Corrosion rate
Temperature (°C)
Corrosion rate (μm/y)
Time (y)
0.1
1
10
100
1000
10⁴
10⁵
10⁶
Magnetite 10,000 y
Magnetite 1 Ma
Siderite 10,000 y
Siderite 1 Ma
Cumulative magnetite precipitation (mol/L)
Cumulative siderite precipitation (mol/L)
Radial distance (dm)
4.5
4.75
5
5.25
5.5
5.75
6

Figure 10